Monthly Notices
of the
ROYAL ASTRONOMICAL SOCIETY

MNRAS **486,** 462–485 (2019)
Advance Access publication 2018 December 20

doi:10.1093/mnras/sty3462

QUIJOTE scientific results – III. Microwave spectrum of intensity and polarization in the Taurus Molecular Cloud complex and L1527

F. Poidevin,[1,2]★ J. A. Rubiño-Martín,[1,2]★ C. Dickinson,[3] R. Génova-Santos,[1,2] S. Harper,[3] R. Rebolo,[1,2] B. Casaponsa,[4] A. Peláez-Santos,[1,2] R. Vignaga,[1,2] F. Guidi,[1,2] B. Ruiz-Granados,[1,2] D. Tramonte,[1,2] F. Vansyngel,[1,2] M. Ashdown,[5,6] D. Herranz,[4] R. Hoyland,[1,2] A. Lasenby,[5,6] E. Martínez-González,[4] L. Piccirillo[3] and R. A. Watson[3]

[1]*Instituto de Astrofisíca de Canarias, E-38200 La Laguna, Tenerife, Canary Islands, Spain*
[2]*Departamento de Astrofísica, Universidad de La Laguna (ULL), E-38206 La Laguna, Tenerife, Spain*
[3]*Jodrell Bank Centre for Astrophysics, Alan Turing Building, School of Physics and Astronomy, The University of Manchester, Oxford Road, Manchester M13 9PL, UK*
[4]*Instituto de Física de Cantabria (CSIC-Universidad de Cantabria), Avda. de los Castros s/n, E-39005 Santander, Spain*
[5]*Astrophysics Group, Cavendish Laboratory, University of Cambridge, J.J. Thomson Avenue, Cambridge CB3 0HE, UK*
[6]*Kavli Institute for Cosmology, University of Cambridge, Madingley Road, Cambridge CB3 0HA, UK*

Accepted 2018 December 17. Received 2018 December 17; in original form 2018 April 24

ABSTRACT

We present new intensity and polarization observations of the Taurus Molecular Cloud (TMC) region in the frequency range 10–20 GHz with the multifrequency instrument (MFI) mounted on the first telescope of the Q-U-I-JOint TEnerife (QUIJOTE) experiment. From the combination of the QUIJOTE data with the *WMAP* 9-yr data release, the *Planck* second data release, the DIRBE maps, and ancillary data, we detect an anomalous microwave emission (AME) component with flux density $S_{\rm AME,peak} = 43.0 \pm 7.9$ Jy in the TMC and $S_{\rm AME,peak} = 10.7 \pm 2.7$ Jy in the dark cloud nebula L1527, which is part of the TMC. In the TMC the diffuse AME emission peaks around a frequency of 19 GHz, compared with an emission peak about a frequency of 25 GHz in L1527. In the TMC, the best constraint on the level of AME polarization is obtained at the *Planck* channel of 28.4 GHz, with an upper limit $\pi_{\rm AME} < 4.2$ per cent (95 per cent C.L.), which reduces to $\pi_{\rm AME} < 3.8$ per cent (95 per cent C.L.) if the intensity of all the free–free, synchrotron and thermal dust components are negligible at this frequency. The same analysis in L1527 leads to $\pi_{\rm AME} < 5.3$ per cent (95 per cent C.L.) or $\pi_{\rm AME} < 4.5$ per cent (95 per cent C.L.) under the same assumption. We find that in the TMC and L1527 on average about 80 per cent of the H II gas should be mixed with thermal dust. Our analysis shows how the QUIJOTE-MFI 10–20 GHz data provide key information to properly separate the synchrotron, free–free, and AME components.

Key words: radiation mechanisms: general – ISM: individual object: Taurus Molecular Cloud, L1527 – diffuse radiation – radio continuum: ISM.

1 INTRODUCTION

Anomalous microwave emission (AME) is a component of Galactic radiation at frequencies of ∼10–60 GHz first detected about 20 yr ago (see Leitch et al. 1997; de Oliveira-Costa et al. 1998). AME strongly correlates with far-infrared (FIR) thermal dust emission almost everywhere in our Galaxy but cannot be explained by synchrotron, free–free, thermal dust, or cosmic microwave background (CMB) emission. The nature of the carriers producing AME is still not known but theory predicts that electric dipole emission from very small, rapidly rotating dust grains could be the origin of this emission (see Draine & Lazarian 1998; Ali-Haïmoud, Hirata & Dickinson 2009; Hoang, Draine & Lazarian 2010; Ysard & Verstraete 2010). Spinning dust models (e.g. Ali-Haïmoud et al. 2009) have been developed and spectral energy distributions (SEDs) inferred from the observations are well described by such models. Magnetic dipole emission is an alternative proposed mechanism to explain AME (see Draine & Lazarian 1999; Draine & Hensley 2013). A review of some observations, mostly at 1-degree resolution, discussed by Génova-Santos et al. (2017) shows that AME is expected to be linearly polarized, if at all, at a very low level.

★ E-mail: fpoidevin@iac.es (FP); jalberto@iac.es (JAR-M)

© 2018 The Author(s)
Published by Oxford University Press on behalf of the Royal Astronomical Society

Downloaded from https://academic.oup.com/mnras/article-abstract/486/1/462/5255197 by CSIC user on 05 June 2020

This could be in agreement with quantum suppression of alignment in very small grains as proposed by Draine & Hensley (2016). Recent studies shed doubt on polycyclic aromatic hydrocarbons (PAHs) being AME carriers (Hensley, Draine & Meisner 2016; Hensley & Draine 2017). On the other hand, high-resolution observations at 11.3 μm in the MWC 1080 Nebula show that some PAHs emit linear polarization at a level of 2 per cent (see Zhang et al. 2017). Such observations leave room for further attempts at high-resolution polarization measurement of AME in different astronomical environments, thus making the origin of AME a much debated subject. A full review on the state of our knowledge of AME and future avenues of research is given by Dickinson et al. (2018).

The Q-U-I-JOint TEnerife (QUIJOTE) experiment is a collaborative project consisting of two telescopes and three linear polarimeters covering the frequency range 10–42 GHz. The main science driver of this project is to constrain or detect the B-mode anisotropy in the CMB polarization down to a tensor-to-scalar ratio of $r = 0.05$. Such a goal is attainable only under the condition that the polarization of the low-frequency foregrounds, mainly the synchrotron and the AME, are well understood. The first instrument of the QUIJOTE experiment, the multifrequency instrument (MFI), observing through bandpasses centred at 11, 13, 17, and 19 GHz has been specifically designed for this purpose. A more detailed description of some of the technical aspects can be found in Rubiño-Martín et al. (2012). The first scientific results obtained with the MFI are presented in Génova-Santos et al. (2015) and Génova-Santos et al. (2017). Recent reviews on the status of the project are detailed in Rubiño-Martín et al. (2017) and Poidevin et al. (2018).

The detection and study in intensity of AME have been investigated towards different types of regions including supernova remnants and planetary nebulae, and several molecular cloud regions (see Planck Collaboration XXV 2016f). A follow-up of a series of molecular clouds in the frequency range 10–20 GHz showing potentially strong AME candidates will be the subject of a future paper. Here we focus on the Taurus Molecular Cloud (TMC) which is the closest and one of the most studied low-mass star-forming regions in our Galaxy. The science driver that leads us to observe the TMC with the QUIJOTE experiment is that the TMC is pervaded by a large-scale uniform magnetic field, as proved from polarization by extinction (e.g. Arce et al. 1998; Chapman et al. 2011) in the visible and near-infrared (NIR), and by emission (e.g. Planck Collaboration XIX 2015a) at submillimetre wavelengths, i.e. from the point of view of thermal dust grains. In addition, the TMC is situated below the Galactic plane at galactic declinations $b < -11°$, which decreases confusion with components associated with the Milky Way. These conditions make this region an interesting laboratory in which to study AME intensity and polarization properties.

The TMC is located at a mean distance of 140 pc with an expected thickness of ∼0.7 pc in the line of sight (Qian et al. 2015) and a total mass of about 1.5 $\times 10^4\,M_\odot$ derived from CO data analysis (Pineda et al. 2010). The L1527 dark cloud nebula is a region located at position $(l, b) = (174.0°, -13.7°)$ where the brightest bulk of thermal dust emission is detected in the TMC. Fig. 1 shows the location of the TMC and L1527 in the field of view of the QUIJOTE MFI instrument. From ^{13}CO observations the TMC as a whole appears to be a complex network of filaments, the width of which follows a broad distribution (Panopoulou et al. 2014). This network of filaments is pervaded by well-structured large-scale magnetic fields as seen from IR (see Chapman et al. 2011) and visible (see Arce et al. 1998) polarization of starlight produced by absorption of dust grains aligned perpendicular to the magnetic field. The large-scale structure of the magnetic fields inferred from these data reveals a picture consistent with the magnetic fields traced with polarized thermal dust emission (see Planck Collaboration XX 2015b). Taking advantage of all the astrophysical information provided by the *Planck* satellite an intensive study of the thermal dust properties is provided by Planck Collaboration XXV (2011b). Thermal dust in equilibrium with the incident radiation field is shown to cool down from 16 to 17 K in the diffuse regions to 13–14 K in the coldest regions. Dust spectral emissivity indices are centred at 1.78 with a standard deviation of 0.08 and a systematic error of 0.07. A study of the spatial variations of the dust optical depth at 250 μm (τ_{250}) shows an increase in $\tau_{250}/N_{\rm H}$ by a factor of about 2 between the atomic phase and the molecular phase, thus attesting radiative transfer effects as the density increases. Additional pictures of certain physical mechanisms have been inferred from the study of specific filaments of the TMC. Ysard et al. (2013) have shown an increase in the FIR dust grain opacity valid along the entire length of the dense filament of L1506 that is interpreted as being due to grain growth and therefore dynamic dust grain evolution. Striations perpendicular to the B211/B213/L1495 filament have been detected by the *Herschel* satellite (see Palmeirim et al. 2013). These structures tend to be aligned with the magnetic field directions and suggest the accretion of material on to the filament.

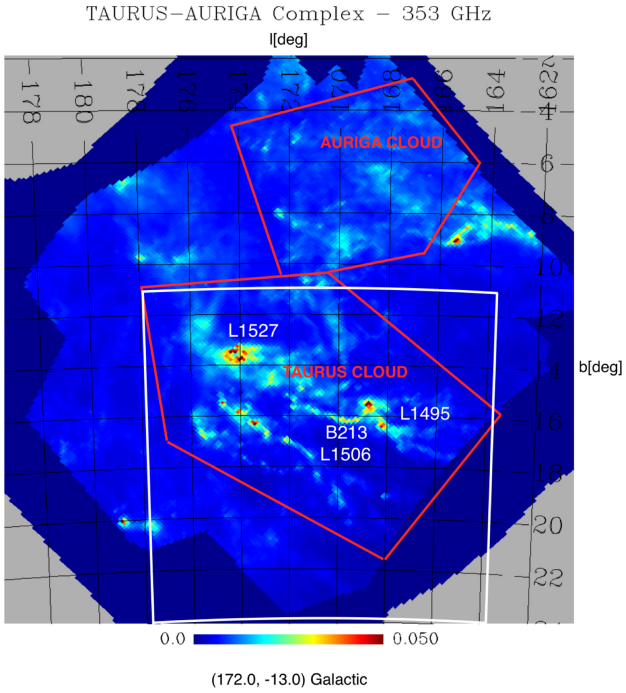

Figure 1. Location of the TMC part of the Taurus–Auriga complex (red boxes) in the field of view common to the four horns of the QUIJOTE MFI instrument displayed on the 353 GHz *Planck* map of thermal dust emission. Our analysis is focussed on the region delineated by the white box.

In this work we present new intensity and polarization measurements of the emission between 10 and 20 GHz with the first instrument of the QUIJOTE experiment towards the Taurus–Auriga complex (see Fig. 1). These measurements have been obtained in order to probe and constrain the level of AME inside the TMC and L1527. At Galactic latitudes $> -11°$ the synchrotron radiation increases substantially in the direction of the Galactic plane. For that reason, in the following, unless specified otherwise, we focus our analysis on the area observed at Galactic latitudes $< -11°$.

Downloaded from https://academic.oup.com/mnras/article-abstract/486/1/462/5255197 by CSIC user on 05 June 2020

We begin by summarizing the data set employed in Section 2. The *Planck* component separation products are compared to the QUIJOTE 13 GHz map and are discussed in Section 3. In Section 4 we analyse the morphology structure of the free–free maps obtained by using the Hα map and compare it to the Commander free–free map. We use a TT-plot analysis to estimate the synchrotron component power law. We show how the QUIJOTE data improve the detection of AME, quantify the amount of AME associated with the TMC and L1527, and then put constraints on the level of polarization of the AME in both regions. The results and the various methods used to estimate the contributions of the synchrotron, free, and AME components are compared and discussed in Section 5. The conclusions are given in Section 6.

2 OBSERVATIONS AND DATA

2.1 QUIJOTE data

The data used in this work were obtained with the first instrument of QUIJOTE, also called the MFI. It consists of four horns that provide eight independent maps of sky intensity and polarization at an angular resolution close to one degree and in four frequency bands centred at 11, 13, 17, and 19 GHz (each frequency is duplicated in two different horns), each with a 2 GHz bandwidth. The data from this instrument have been used for the first time to analyse the intensity and polarization properties of the AME in the Perseus molecular complex (Génova-Santos et al. 2015). A similar analysis was conducted with data obtained towards the molecular complexes W43 and W47 and towards the supernova remnant W44 (Génova-Santos et al. 2017). This analysis provides the most stringent constraints on the level of AME polarization associated with a molecular cloud structure with $\pi_{\rm AME} < 0.39$ per cent (95 per cent C.L.) from QUIJOTE 17 GHz data and $\pi_{\rm AME} < 0.22$ per cent (95 per cent C.L.) from *WMAP* 41 GHz data. Here we present new data obtained towards the TMC.

2.1.1 *Observations and basic data processing*

The observations used in this work were carried out from 2015 March 4 to 2015 July 27 using the MFI. They consisted of raster scans at constant elevation in local coordinates centred on the TMC complex. We performed the observations by scanning the sky in azimuth over a range of 15° at a constant elevation and at a velocity of 1° in sky coordinates, stepping the elevation by 0.1° after each scan. Each of these observations took around 25 min and produced a map of the sky capturing the transient of the TMC at the elevation defined as a function of the time of observation. The MFI horns point to sky positions separated by up to 5°, so each horn rasters a slightly different patch. Therefore, the total sky area surveyed in each of these observations is slightly wider. Once all the observations are combined together, the area common to all the horns is about $\sim 17^\circ \times 17^\circ$ (see Fig. 1).

The final observing time was of 451 h. All the data were first carefully inspected by eye. Data affected by out-of-range housekeeping values, contamination by geostationary satellites and their near-sidelobes imprints, and transient sources such as the sun, moon, and planets were automatically removed at the pipeline level and not used in this study. All data less than 5° from any satellite on the plane of the sky were also automatically removed. The data showing glitch-type variations, radio frequency interference (RFI), and any uncommon variations in the calibrated time-ordered-data (CTOD), including rapid atmospheric variations, that might produce strong signal variations were also removed. For this purpose a model of the sky (Harper et al. 2018) was removed from each of the 32 CTODs and the dispersions in groups of data of size 8 s were calculated for all the data. All groups of data of size 8 s with a dispersion higher than a threshold value were flagged as bad data and not included when producing the final maps. The remaining calibrated data not flagged at the CTOD level were stacked as a function of azimuth in bins of one third of a degree. Additional flagging was applied by identifying ranges of azimuth where the stacked data still showed high values. For horn 2 17 GHz maps we directly identified by eye the TOD pausing problems by looking at the stacked data and removing the full CTODs from the analysis. After flagging, the final effective observing time in the area common to all the horns is of about 290, 272, 281, and 241 h, for horns 1, 2, 3, and 4, respectively. Horns 1 and 3 provide the 11 and 13 GHz bands. They are less affected by unstable channels than horns 2 and 4 but are more sensitive to external RFI signals entering through far side lobes from geostationary satellites. Horns 2 and 4 are expected to be less sensitive to RFI contamination. The filtering process to remove groups of data contaminated by spurious signals is working well but horn 4 was particularly exposed to an unidentified source of RFI during the observations of the TMC which results in high RMS values in some areas of the maps thereby rendering them of limited use for science. For this reason all the maps from horn 4 are not used in our analysis. As will be discussed in more detail below, the noise levels in intensity are in the range 40–120 μJy $(1^\circ \text{ beam})^{-1}$ and 3–5 times lower in Q and U.

2.1.2 *Calibration*

Our calibration process is similar to the one explained in Génova-Santos et al. (2017). The main calibrator is Cass A, whose flux scale is assumed to follow that derived by Weiland et al. (2011) with *WMAP* data. The secular variation of CASS A is taken into account and corrected for by using the model proposed by Hafez et al. (2008). The amplitude calibrator Cass A was observed at least once a day except on a few days when observations had to be stopped owing to brief intervals of poor weather. A total of 230 individual Cass A observations were obtained during the period of observations of the TMC and the averaged gain calibration factors are calculated for all the Cass A data obtained between 2014 April and 2015 December. The scatter in the distribution of the measured gain factors for the 32 channels is in the range 0.3–2.2 per cent and is on average around 0.7 per cent. An improvement with respect to the previous calibration (Génova-Santos et al. 2015, 2017) is that the pipeline now takes advantage of the calibration diode installed in the middle of the secondary mirror in front of the MFI. This diode is switched on for one second every 31 s and is used to track gain variations over time-scales of 30 min for horns 1 and 3, and of 1 h for horns 2 and 4. The median value of the calibration factors calculated for each channel were modulated as a function of time by these variations and then used to calibrate each observation of Taurus. The errors due to the secular variations of Cass A, as well as the errors from the extrapolation of the Cass A fluxes at *WMAP* and *Planck* frequencies to the QUIJOTE frequencies of order 4 per cent, were added in quadrature to the gain calibration errors. All in all, we conservatively estimate that our absolute calibration errors are accurate to within 5 per cent for each channel.

The reference zero position angles of the modulator for each horn of the MFI were estimated by using Tau A (Crab Nebula)

Downloaded from https://academic.oup.com/mnras/article-abstract/486/1/462/5255197 by CSIC user on 05 June 2020

observations. Tau A was observed at least on every day the Taurus region was observed. The polarization angle of Tau A, estimated at 22.8 GHz by Weiland et al. (2011), varies by less than 5 per cent from 22.7 to 90 GHz. We assume the same to be true, or better, in the frequency range of the MFI. We checked that the reference position angles remained constant over time and found the scatter of the measurements to be lower than 1 per cent. We then combined all the results from the individual observations and derived the final values used for each horn. The statistical accuracy of the values is of the order of a tenth of a degree for each horn.

2.1.3 *Map making*

The optics of the first QUIJOTE telescope provide highly symmetric beams (ellipticity >0.98) with very low sidelobes ($\lesssim -40$ dB) and polarization leakage ($\lesssim -25$ dB). The MFI has been modified a few times since its first light. The half-wave plate was blocked to position A (i.e. 0° in the reference frame of the half-wave plate) from 2013 September, and for that reason the polarization maps of this horn are not used. As a test bed horn 1 was modified during 2014 April and all its paired channels have been correlated from that time. Further modifications of the instrument took place in 2015 December in order to get all the pairs of channels of horns 2, 3, and 4 correlated. For horns 2, 3, and 4, of the four channels per frequency range two channels were correlated and two were still uncorrelated during the Taurus observations. In intensity the typical knee frequencies are of order $f_k \sim 10$–40 Hz depending on the channel. The correlated channels are those used to calculated the Q and U maps because, for the measurement of polarization the subtraction results in much lower values of $f_k \sim 0.1$–0.2 Hz. The method of deriving the values of the I, Q, and U Stokes parameters is therefore the same as that used by Génova-Santos et al. (2017), and we refer the reader to this article for more details.

The final maps were produced with a destriper map-maker implemented at the IAC and used to lower the stripes produced by the scanning strategy (e.g. Kurki-Suonio et al. 2009). Because of the low fraction of the sky (with respect to the full sky) covered by the observations a gradient perpendicular to the direction of the scans was present in the QUIJOTE intensity maps. This effect was removed a posteriori by removing a two-dimensional plane from the final maps. As a consistency test, the same procedure was applied to the *WMAP* 22.8 GHz and showed a null residual between the original and corrected map over the area of interest, thereby attesting that the origin of the gradient observed in the QUIJOTE maps came from residual baseline drifts and RFI signals propagating into the maps as smoothed gradients. Our final maps use the HEALPIX format [for Hierarchical Equal Area isoLatitude Pixelization (HEALPix) of a sphere Górski et al. 2005] with $N_{\rm side} = 512$ (i.e. a pixel size of $\lesssim$6.9 arcmin) that is sufficient enough to sample our beam. For further comparisons and combinations all our maps were smoothed with a kernel corresponding to an angular full width at half-maximum (FWHM) of 1°.

2.2 QUIJOTE maps of the Taurus Molecular Clouds

The intensity maps from horn 1 (11 and 13 GHz), horn 2 (17 and 19 GHz), and horn 3 (11 and 13 GHz) are used for our analysis. As mentioned previously, the intensity maps obtained with horn 4 lack sensitivity because many data had to be flagged out because of the presence of RFIs during the observations. The polarization maps from horn 3 are also used for our analysis. The polarization maps from horn 4 are discarded because of the problem with the intensity maps. The polarization maps from horn 1 are also not used because of the lack of definition to reconstruct Stokes Q and U parameters. The sensitivities of all the I, Q, and U maps from the correlated channels are given in Table 1. The sensitivities of the I destriped maps are in the sensitivity range $\approx$ 40–120 μK beam^{-1} to a resolution of 1°. Given the low cut-off of the 1/f noise the sensitivies of the Q and U maps are three to five times better than those from the intensity maps. NTs have been implemented that show consistency between the different data sets (see Table 1 and additional tables in Appendix A) and ensure low-level contamination by RFIs above the detector nominal sensitivities in data from horns 1, 2, and 3. The I, Q, and U maps obtained with the MFI at 11 and 13 GHz with horn 3, and at 17 and 19 GHz with horn 2 are shown in Fig. 2 and are compared with the maps obtained by *WMAP* at 22.7 GHz.

2.3 Ancillary and survey data

The turnover of the AME spectral energy distribution is on average expected to be detected at frequencies lower than 30 GHz, including the frequency range 10–20 GHz in which the QUIJOTE MFI observes. In order to fully sample the spectrum and the turnover of the AME SED the *Planck* (28.5, 44.1, and 70.3 GHz, 2015 release) and *WMAP* 9-yr (22.8, 33.0, 40.7, and 60.7 GHz) low-frequency maps are added to our data. The *WMAP* 9-yr and *Planck* HFI maps at frequencies higher than 90 GHz and the low-frequency DIRBE maps (100, 140, and 240 μm) are combined together to characterize the contribution of the thermal dust that dominates at frequencies higher than ≈100 GHz. On the other side of the spectrum, at very low radio frequency, ancillary data are used to characterize the respective contributions of the synchrotron and free–free emissions.

All the data used in our analyses and the surveys they have been obtained from are summarized in Table 2. We use the most up to date version of these maps regridded into the HEALPIX format (Górski et al. 2005) at $N_{\rm side} = 512$. All the maps were smoothed to a common resolution of 1°. Some of the maps show significant baseline, or offset, uncertainties, but we circumvent this problem by using T–T plots (Turtle et al. 1962), or by removing these offsets by subtracting a local background in each map when conducting SED analyses. In the following section we discuss some of these data in more detail.

2.3.1 *Low-frequency ancillary data*

At low frequencies we use the all-sky 408 MHz map of Remazeilles et al. (2015), and the Reich & Reich (1986) I map and Wolleben et al. (2006) Q and U maps at 1.420 GHz. The map provided by Remazeilles et al. (2015) is an improved version of the total-power radio survey map of Haslam et al. (1982). Various corrections have been applied to improve the original four individual maps by using filtering techniques. The most notable corrections include the reduction to a level $\ll$1 K of large-scale striations associated with 1/f noise in the scan direction and the removal of the brightest extragalactic sources ($\gtrsim$2 Jy). In order to take into account the power that is introduced through the sidelobes in the 1.420 GHz map we apply the correction factor of 1.55 derived by Reich & Reich (1988) to compensate for the initial calibration of the map that was referred to the full-beam solid angle. We assume a 10 per cent uncertainty in the radio data at these two frequencies.

Downloaded from https://academic.oup.com/mnras/article-abstract/486/1/462/5255197 by CSIC user on 05 June 2020

Table 1. RMS per 1° beam in intensity and polarization, calculated on the QUIJOTE maps in a circular aperture of diameter 1° around Galactic coordinates $(l, b) = (167°, -13°)$. For each Stokes parameter (I, Q, U) we show the RMS estimated from the original maps and from half the difference of the two null test (NT) maps as a function of Julian date. The RMS obtained from the original maps should be representative of the combined background and instrumental noise uncertainties, whereas the RMS calculated from the combination of the NT maps should be indicative of the level of instrumental noise only. In the last column we display the instrument instantaneous sensitivities in polarization obtained by normalizing the averaged Q and U noise estimates calculated from the NT maps by the averaged integration time per beam.

Horn	Freq. (GHz)	σ_I (μK beam^{-1})		σ_Q (μK beam^{-1})		σ_U (μK beam^{-1})		$\sigma_{Q,U}$ (mK s$^{1/2}$)
		Map	NT	Map	NT	Map	NT	NT
1	11	45.9	29.6	–	–	–	–	–
1	13	38.5	25.2	–	–	–	–	–
2	17	98.0	63.3	16.1	12.0	15.1	12.7	2.8
2	19	115.0	78.5	21.9	16.2	16.6	14.6	2.9
3	11	70.9	49.2	21.4	14.1	15.1	12.6	2.6
3	13	58.2	37.6	18.7	12.6	16.5	11.8	2.3
4	17	103.4	71.9	18.1	11.9	14.4	11.2	2.2
4	19	122.0	82.4	21.5	16.2	19.3	19.1	3.3

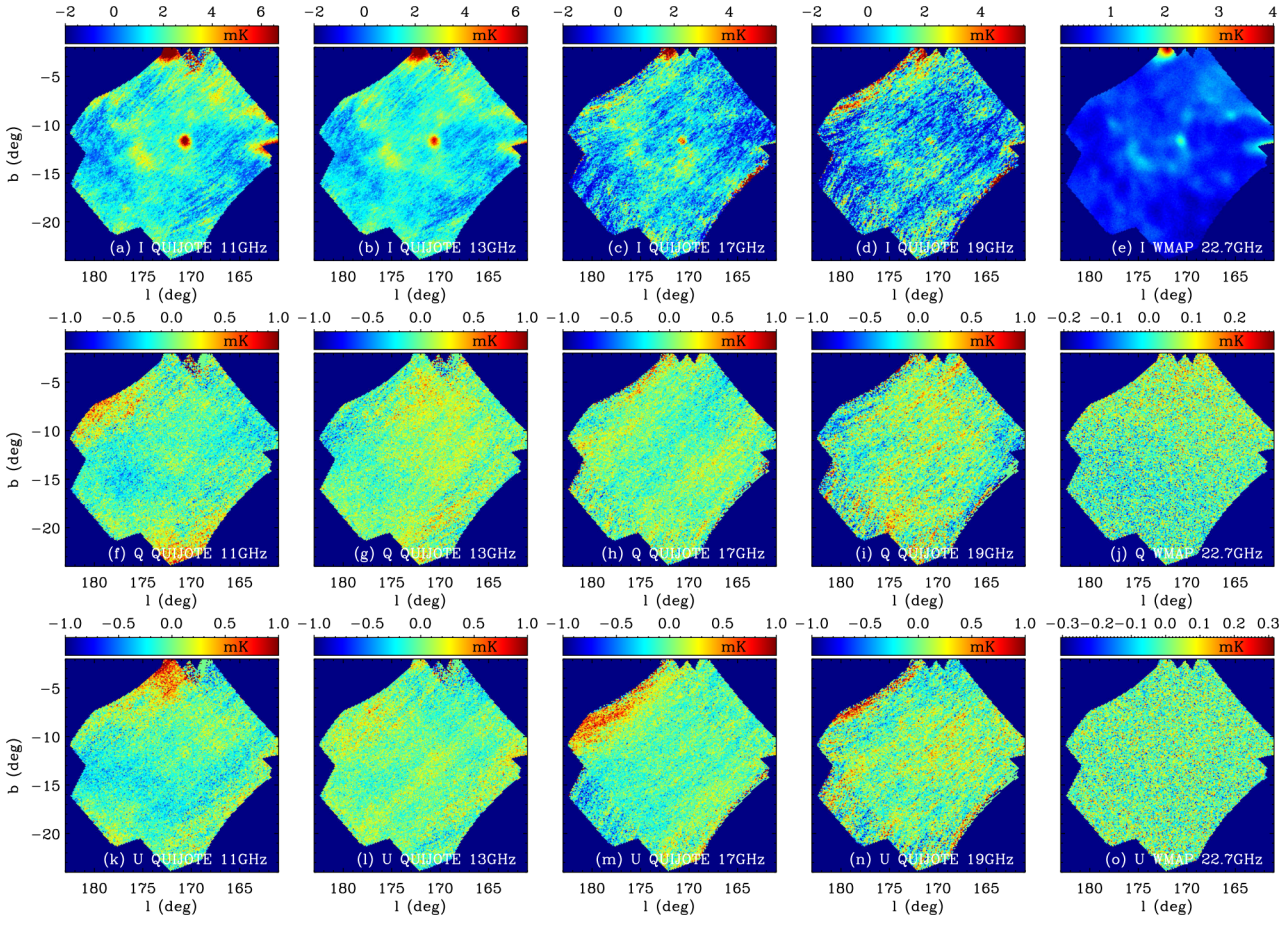

Figure 2. Top row: intensity maps of the Taurus region observed with horn 3 of the MFI at a frequency of 11 GHz (a), 13 GHz (b), with horn 2 at a frequency of 17 GHz (c) and 19 GHz (d), and with *WMAP* at 22.7 GHz (e). Second row: Stokes parameter Q maps observed with horn 3 of the MFI at a frequency of 11 GHz (f), 13 GHz (g), 17 GHz (h), 19 GHz (i) and with *WMAP* at 22.7 GHz (j). Third row: Stokes parameter U maps observed with horn 3 of the MFI at a frequency of 11 GHz (k), 13 GHz (l), 17 GHz (m), 19 GHz (n), and with *WMAP* at 22.7 GHz (o).

Downloaded from https://academic.oup.com/mnras/article-abstract/486/1/462/5255197 by CSIC user on 05 June 2020

Table 2. List of surveys and maps used in our analysis.

Frequency (GHz)	Wavelength (mm)	Telescope/ survey	Angular resolution (arcmin)	Stokes parameters	Units	References
0.408	735.42	JB/Eff/Parkes	≈60	*I*	[K_{RJ}]	Haslam et al. (1982) Remazeilles et al. (2015)
1.420	211.30	Stockert/Villa-Elisa	36	*I*, *Q*, *U*	[K_{RJ}]	Reich (1982) Reich & Reich (1986) Reich, Testori & Reich (2001) Wolleben et al. (2006)
22.8	13.16	*WMAP* 9-yr	≈49	*I*, *Q*, *U*	[mK_{CMB}]	Bennett et al. (2013)
28.5	10.53	*Planck* LFI	32.60	*I*, *Q*, *U*	[K_{CMB}]	Planck Collaboration I (2016b)
33.0	9.09	*WMAP* 9-yr	≈40	*I*, *Q*, *U*	[mK_{CMB}]	Bennett et al. (2013)
40.7	7.37	*WMAP* 9-yr	≈31	*I*, *Q*, *U*	[mK_{CMB}]	Bennett et al. (2013)
44.1	6.80	*Planck* LFI	27.92	*I*, *Q*, *U*	[K_{CMB}]	Planck Collaboration I (2016b)
60.7	4.94	*WMAP* 9-yr	≈21	*I*, *Q*, *U*	[mK_{CMB}]	Bennett et al. (2013)
70.3	4.27	*Planck* LFI	13.01	*I*, *Q*, *U*	[K_{CMB}]	Planck Collaboration I (2016b)
93.5	3.21	*WMAP* 9-yr	≈13	*I*	[mK_{CMB}]	Bennett et al. (2013)
100	3.00	*Planck* HFI	9.37	*I*	[K_{CMB}]	Planck Collaboration I (2016b)
143	2.10	*Planck* HFI	7.04	*I*	[K_{CMB}]	Planck Collaboration I (2016b)
217	1.38	*Planck* HFI	4.68	*I*	[K_{CMB}]	Planck Collaboration I (2016b)
353	0.85	*Planck* HFI	4.43	*I*, *Q*, *U*	[K_{CMB}]	Planck Collaboration I (2016b)
545	0.55	*Planck* HFI	3.80	*I*	[MJy sr^{-1}]	Planck Collaboration I (2016b)
857	0.35	*Planck* HFI	3.67	*I*	[MJy sr^{-1}]	Planck Collaboration I (2016b)
1249	0.24	*COBE*-DIRBE	≈40	*I*	[MJy sr^{-1}]	Hauser et al. (1998)
2141	0.14	*COBE*-DIRBE	≈40	*I*	[MJy sr^{-1}]	Hauser et al. (1998)
2997	0.10	*COBE*-DIRBE	≈40	*I*	[MJy sr^{-1}]	Hauser et al. (1998)

2.3.2 *WMAP data*

In the microwave range, at frequencies 23, 33, 41, 61, and 94 GHz, we use the *I*, *Q*, and *U* maps from the 9-yr data release of the *WMAP* satellite (Bennett et al. 2013). All the maps were retrieved from the LAMBDA database.[1] Towards the TMC the maps are not dominated by instrumental noise and we assume a 3.2 per cent overall calibration uncertainty.

2.3.3 Planck *HFI and LFI data*

Additional *I*, *Q*, and *U* maps are available in the microwave range at frequencies 28, 44, and 70 GHz. They were obtained with the low-frequency instrument (LFI) on board of the *Planck* satellite (Planck Collaboration I 2016b). We use the second public release version of these maps as provided by the *Planck* Legacy Archive (PLA[2]). The LFI maps were corrected for the bandpass mismatch, which produces intensity to polarization leakage, by using the correction maps also provided at $N_{side} = 256$ in the PLA database.

In the submillimetre (submm) range we use the second data release version of the intensity maps obtained with the high-frequency instrument (HFI) on board the *Planck* satellite (Planck Collaboration I 2016b) at frequencies centred at 100, 143, 217, 353, 545, and 857 GHz. The type 1 CO maps (Planck Collaboration XIII 2014d) were used to correct the 100, 217, and 353 GHz intensity maps for contamination introduced by the CO rotational transition lines (1–0), (2–1) and (3–2), respectively. Stokes parameter *Q* and *U* maps were obtained with the HFI at 100, 143, 217, and 353 GHz. The second release version of the *Planck* maps show a non-negligible leakage problem in the *Q* and *U* maps at 100, 143, and 217 GHz; therefore, in our analysis we only use the 353 GHz *Q* and *U* maps. We assume an overall calibration uncertainty of 3.4 per cent in the HFI and LFI data at frequencies lower than 217 GHz, but a value of 10 per cent at 353, 545, and 857 GHz.

2.3.4 *High-frequency ancillary data*

In the FIR range we use the Zodi-Subtracted Mission Average (ZSMA) *COBE*-DIRBE maps (Hauser et al. 1998) at 240 μm (1249 GHz), 140 μm (2141 GHz), and 100 μm (2997 GHz). We assume an 11.9 per cent overall calibration uncertainty in the data at these frequencies.

2.3.5 *Colour corrections*

Map colour corrections were applied to all the surveys except for those at frequencies 0.408 and 1.420 GHz, for which the narrow bandwidths of the detectors make the corrections negligible. The colour correction dependence on the fitted models was taken into account by implementing an iterative process (e.g. Planck Collaboration IX 2014b). In each iteration the fitted model on the QUIJOTE, *WMAP*, and *Planck* maps is integrated over the bandpasses retrieved from the QUIJOTE calibration database, the LAMBDA archive, and the PLA, respectively. In the case of the DIRBE survey we use the colour correction tables provided by the LAMBDA archive. The convergence is generally fast and is reached after the second or third iteration. The magnitude of the colour corrections is $\lesssim$1.3 per cent for the QUIJOTE maps, $\lesssim$3.1 per cent for the *WMAP* maps, and $\lesssim$12.2 per cent for the *Planck* and DIRBE maps.

[1]Legacy Archive for Microwave Background Data Analysis, http://lambda.gsfc.nasa.gov/.
[2]*Planck* Legacy Archive (PLA) http://pla.esac.esa.int/pla/.

Downloaded from https://academic.oup.com/mnras/article-abstract/486/1/462/5255197 by CSIC user on 05 June 2020

3 PLANCK COMPONENT SEPARATION PRODUCTS

Before analysing the set of maps obtained from direct observations of the sky, we consider various templates providing estimates of several physical components. These maps were produced with the Commander component separation algorithm (Planck Collaboration XXV 2016f) and are by-products of various maps listed in Table 2. Among other foreground maps we use the emission measure (EM) and electron temperature templates that provide information relative to the level of free–free emission. Hints on the level of emission of AME and the level of synchrotron emission expected towards the Taurus region are given in the AME and synchrotron Commander templates respectively. In the frequency range where thermal dust emission is the major component we use the optical depth estimates provided by the template at 545 GHz. All the maps were retrieved from the PLA.

3.1 Commander maps

The maps discussed in this section are the products of the Commander component separation algorithm (Planck Collaboration X 2016d). This tool uses Monte Carlo/Markov chains in a Bayesian framework to explore a parametrized description of the foregrounds. In the data model, each foreground is described by a template map at a given frequency and a spatially dependent SED. The parametric model of the SED depends on the foreground under consideration. It has been used on combinations of the Haslam et al. (1982) 408 MHz, *WMAP*, and *Planck* maps to investigate the range of spectral indices and morphologies at frequencies around 20–50 GHz. The products of this analysis are a CMB-nulled map at 22.8 GHz. One of the CMB maps obtained from the analysis of the diffuse foregrounds is the SMICA map, which was obtained using a non-parametric method in the spherical harmonic domain (see Cardoso et al. 2008; Planck Collaboration IX 2016c), where the foregrounds were modelled as a small number of templates. SMICA was the method that performed best on the simulated temperature data. We use the SMICA CMB map to subtract the CMB component directly at the map level. The GALPROP model (Strong, Orlando & Jaffe 2011; Orlando & Strong 2013) is used to estimate the synchrotron emission and produce full-sky maps of the free–free electron temperature and EM, and two AME component maps at 22.8 and 41.0 GHz, respectively. The use of GALPROP is based on physically motivated calculation since it requires less parameter tuning than other methods, this to the cost of losing flexibility in tracing real spatial variations. As a consequence, some cross-talk between the synchrotron, free–free, and AME is expected. A thermal dust emission map at a central frequency of 545 GHz is also provided by the analysis.

3.2 AME morphology of the TMC at 13 GHz from Commander

We first estimate the contributions of the free–free, synchrotron, and thermal dust from the Commander component maps at a central frequency of 13 GHz. Assuming a power-law relation (Platania et al. 1998) with a constant index of $\beta_{\rm synch} = 2.8$ (the choice of this value will be justified in Section 4) an average estimate of the level of synchrotron emission at 13 GHz can be obtained by assuming that the Haslam map at 408 MHz mainly probes the synchrotron radiation. The free–free intensity map is estimated at 13 GHz following the equations in table 4 from Planck Collaboration X (2016d) by using the Commander free–free electron temperature

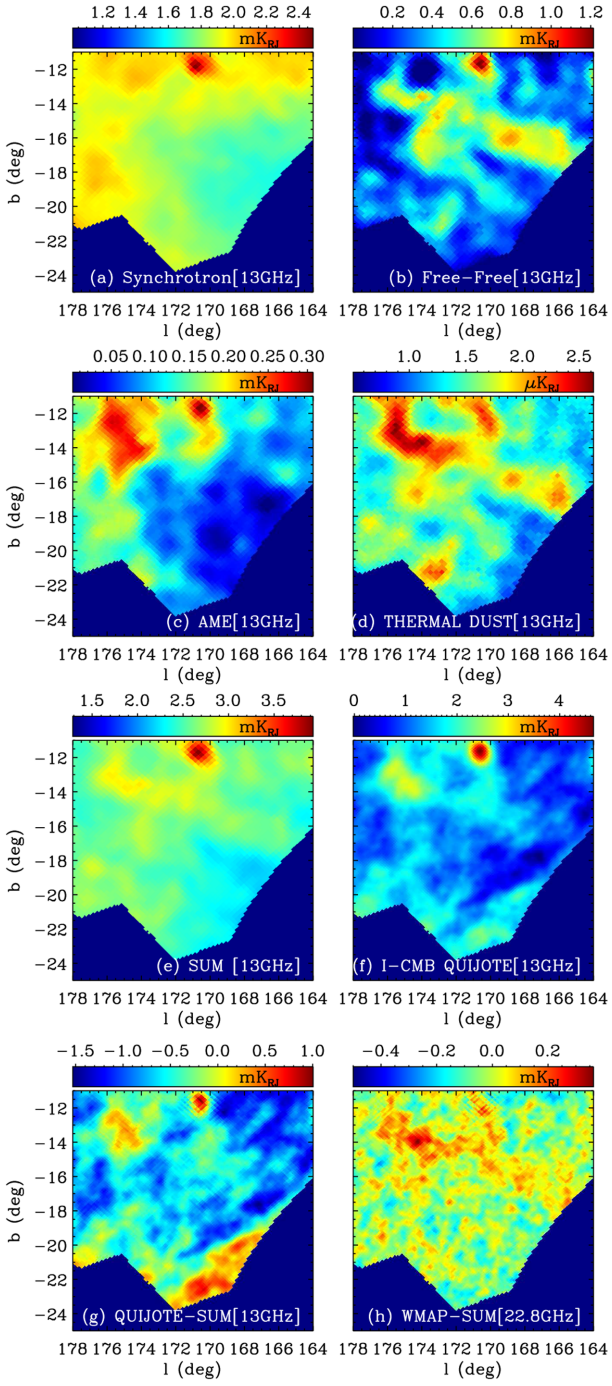

Figure 3. Commander template maps extrapolated to 13 GHz. Top left to bottom right: (a) synchrotron intensity map from the Commander component separation tool (Planck Collaboration XXV 2016f) in $\mathrm{mK_{RJ}}$ at a reference frequency of 13 GHz; (b) free–free intensity map at 13 GHz calculated with the Commander electron temperature and EM maps; (c) Commander AME total intensity map at 13 GHz; (d) thermal dust intensity map in $\mu\mathrm{K_{RJ}}$ from Commander extrapolated from the reference frequency 545 GHz to a frequency 13 GHz; (e) sum map of the synchrotron, free–free, AME, and thermal dust Commander intensity maps at a reference frequency of 13 GHz; (f) QUIJOTE-MFI 13 GHz SMICA-CMB corrected map; (g) QUIJOTE-MFI 13 GHz SMICA-CMB corrected map – Commander 13 GHz Summed maps; and (h) *WMAP* 22.8 GHz SMICA-CMB corrected map – Commander 22.8 GHz summed maps.

Downloaded from https://academic.oup.com/mnras/article-abstract/486/1/462/5255197 by CSIC user on 05 June 2020

Table 3. Name and Galactic positions of the Galactic and extra-Galactic sources located in the field of view (FOV) of the Taurus–Auriga molecular cloud complex (Fig. 1) identified with the second *Planck* CCS (Planck Collaboration XXVI 2016g). The FWHMs are the effective FWHMs from Gaussian fits to the sources.

Source name	Glon (°)	Glat (°)	FWHM (arcmin)	30 GHz flux (mJy)	Other name[a]	Source type[a]
PCCS2 030 G163.79-11.99	163.789	−11.986	33.08	774.27 ± 26.14	1RXS J041435.6 + 341842	X-ray source
PCCS2 030 G168.02-19.65	168.023	−19.653	33.38	1415.45 ± 38.46	QSO B0400 + 258	Quasar
PCCS2 030 G169.00-22.47	169.002	−22.473	33.22	724.52 ± 47.36	IRAS 03542 + 2311	Infra-red source
PCCS2 030 G170.54-11.64	170.544	−11.636	35.89	3867.93 ± 23.38	CXOSEXSI J043659.1 + 294231	X-ray source
PCCS2 030 G171.34-14.38	171.338	−14.378	33.85	1169.57 ± 23.18	2MASS J04294819 + 2717322	Infra-red source
PCCS2 030 G176.90-18.56	176.901	−18.556	32.77	577.59 ± 15.43	2MASS J04313041 + 2035383	T Tau-type star

Note. [a]Information retrieved from the Simbad database (http://simbad.u-strasbg.fr/simbad//). The other name is the one of the closest sources at a distance less than 5 arcmin from the Galactic coordinates given in columns 2 and 3.

Table 4. Power-law index from the *T*–*T* plots between the maps at 408 MHz and 1.420 GHz for several regions considered for cases of free–free emission estimates included in or removed from the maps. The definitions of the regions refer to Fig. 1.

Region	Free–free[a]	$\beta_{\rm synch} \pm \sigma(\beta_{\rm synch})$
Full region	Included	-2.77 ± 0.22
Full region	Removed ($f = 0.8$)	-2.81 ± 0.26
$-11^\circ < b < -2^\circ$	Removed ($f = 0.8$)	-2.71 ± 0.26
$-24^\circ < b < -11^\circ$	Removed ($f = 0.8$)	-2.80 ± 0.26
TMC region[b]	Included	-2.80 ± 0.26
TMC region[b]	Removed ($f = 0.8$)	-2.80 ± 0.26

Notes. [a]80 per cent of the H II gas is assumed to be mixed with thermal dust. [b]TMC region as delineated in white in Fig. 1.

map and EM map. The distribution of the Commander total AME intensity map estimated towards the TMC is obtained by summing the contribution of the two AME component maps provided by the Commander component separation analysis at a central frequency of 13 GHz. The thermal dust intensity map extrapolated from a frequency 545–13 GHz is obtained by following the equations given in table 4 from Planck Collaboration X (2016d). All these maps, as well as their sum, are shown in Fig. 3 for comparison with the 13 GHz MFI CMB-corrected intensity map also displayed in the figure. The CMB correction was done by subtracting the SMICA-CMB map from the QUIJOTE 13 GHz map.

From the Commander component analysis one can see that the synchrotron (panel a) and free–free (panel b) components could respectively contribute about 50 per cent and about 25 per cent or more to the 13 GHz MFI CMB-corrected intensity map. As expected, the thermal dust contribution (panel d) should be fully negligible at this frequency, whereas the AME intensity (panel c) is expected to contribute about 10 per cent of the total intensity. In terms of morphology one can see that the AME is expected to be encountered almost everywhere except in the south-west corner of the Commander map. At first sight the morphology of the sum of the Commander intensity maps (panel e) and the QUIJOTE CMB-corrected intensity map (panel f) look slightly different. In particular the L1495 filament (see Fig. 1) seems to be captured by the Commander free–free component map but is barely seen in the QUIJOTE CMB-corrected intensity map. This discrepancy and others are easier to visualize once one looks to the difference between the QUIJOTE CMB-subtracted map and the Commander summed maps at 13 GHz. This is shown in panel g. Even though the absolute baseline level of the QUIJOTE maps is not known, one can see that the difference map shows strong morphological differences that are not only noise-like. A possible explanation of such differences is that sky maps at the QUIJOTE-MFI frequencies were not available when the Commander analysis was performed. The Commander analysis was performed using the 408 MHz map combined with a set of maps with frequencies higher than 22 GHz. For that reason, it most probably offers a reasonable component separation model at frequencies higher than 22 GHz, but its predictability at frequencies lower than 22 GHz could be limited. As a simple test, we repeated at a frequency of 22.8 GHz the analysis we did at 13 GHz. The structural features obtained at 22.8 GHz (not shown here) are very similar to those seen at 13 GHz (Fig. 3, panels a–e). Indeed, the difference map obtained at 22.8 GHz and shown in panel h is more consistent with noise than that obtained at 13 GHz (panel g). Some residuals of the structure of the molecular clouds can still be seen, though, that may be indicative of cross-talk between the free–free, AME, and synchrotron components at 22.8 GHz. Comparisons between the Commander products and the component separation analysis obtained from spectral energy distributions will be discussed further in Section 5.

3.3 Extra-Galactic sources and masks

Extra-Galactic and Galactic compact sources strongly emitting at 30 GHz and lying in the field of view (FOV) of the TMC complex could bias our analysis. In order to identify and mask these sources we use the *Planck* catalogue of compact sources (CCS) (Planck Collaboration XXVI 2016g). Names identifying sources and their coordinate positions in the Galactic reference frame are given in Table 3. The Gaussian effective FWHM and the 30 GHz fluxes provided by the CCS catalogue are also displayed. Additional information retrieved from the Simbad database is given in the last two columns. The information provided by the CCS was crossed-checked with a search of the NASA/IPAC Extragalactic Database (NED[3]) showing that PCCS2 030 G170.54-11.64 is the well-studied object also known as 3C 123. A closer look at the observations of this source suggested a large-scale structure around 3C 123 with two hotspots about 1° degree away (Reich, Kalberla & Neidhoefer 1976). From comparisons with the extensions seen in the Haslam and QUIJOTE maps we saw that the angle formed by the large-scale hotspots in the map displayed by Reich et al. (1976) are not aligned with the extensions seen in the Haslam and QUIJOTE maps, which look rather circular. Actually, a closer look at the NRAO VLA Sky Survey (NVSS[4]) shows some fairly bright extra-Galactic sources

[3]https://ned.ipac.caltech.edu/.
[4]http://www.cv.nrao.edu/nvss/.

Downloaded from https://academic.oup.com/mnras/article-abstract/486/1/462/5255197 by CSIC user on 05 June 2020

(compact) at these locations, therefore the extension seen in Reich et al. (1976) is not that of giant radio structures. Given the fair amount of extinction in the visible (of order 3 mag) towards 3C 123, we therefore concluded that this source is indeed a bright compact (≈40 arcsec) extra-Galactic radio source sitting on top of an extended Galactic dust cloud. This result agrees with the 1400 MHz data analysis of 3C 123 by Hanisch (1984). In the following, in order to exclude the extra-Galactic or Galactic compact sources in our analysis of the series of 1° resolution maps we apply masks with discs of radius 90 arcmin for PCCS2 030 G170.54-11.64 and 45 arcmin for all the other sources. Some of the masked sources are encountered towards the TMC, as can be seen in the maps shown in Fig. 5.

3.4 Correlation plots in the TMC region

Diffuse AME detection is discussed in Macellari et al. (2011) and is shown to be clearly detected over a large fraction of the sky away from the Galactic plane in the *WMAP K* and K_a. More specific diffuse AME regions are discussed in Planck Collaboration XXV (2016f) including the molecular cloud regions R CrA, ρ Oph, and Musca. In this work the Commander map AME emissivities at 22.8 GHz relative to the thermal dust amplitude at 545 GHz, the IRAS map at 100 μm, and the optical depth at 353 GHz, τ_{353} are discussed. On the galactic scale correlations are found to be higher between AME at 22.8 GHz relative to the thermal dust amplitude at 545 GHz and the optical depth at 353 GHz, τ_{353} than between AME at 22.8 GHz relative to the *IRAS* map at 100 μm (see fig. 12 in Planck Collaboration XXV 2016f). For comparison, we applied a similar analysis to the 1°-resolution Taurus Commander maps with a pixelization at $N_{\rm side} = 64$ including the masks discussed above in the region delineated with a white border in Fig. 1. For each map this pixelization is used to avoid any correlation between pixels. Our results are shown in the plots in Fig. 4. The best correlation is that for the AME emissivities at 22.8 GHz relative to the *IRAS* map at 100 μm with a slope = $31.9 \pm 1.6\,\mu{\rm K_{RJ}}\ ({\rm MJy\,sr^{-1}})^{-1}$ and a correlation factor $r = 0.85$. In comparison, lower correlation factors are found between the AME emissivities at 22.8 GHz relative to the thermal dust amplitude at 545 GHz ($r = 0.46$) and the optical depth at 353 GHz, $\tau_{353} \times 10^6$ ($r = 0.48$). This correlation between the Commander AME product and the 100 μm map suggests that for the TMC the AME carriers could be very small grains, consistently with previous analyses on other regions (see Dickinson et al. 2018, and references therein). For the TMC the correlation factor between the AME emissivities at 22.8 GHz relative to the thermal dust amplitude at 545 GHz are lower than those found for the Pegasus Plume ($r = 0.68$), Musca ($r = 0.63$), and λ Orionis ($r = 0.85$) regions (see fig. 14 in Planck Collaboration XXV 2016f). On the other hand, the AME emissivity to thermal dust optical depth ratio is quite low and of order $2.6 \times 10^{-6}\,\mu{\rm K_{RJ}}$, similar to estimates obtained towards other molecular cloud regions such as ρ Oph and Perseus (see table 2 in Planck Collaboration XXV 2016f).

4 DATA ANALYSIS

Before investigating any SEDs of the intensities mapped towards the Taurus region we take advantage of the low-frequency map and the publicly available Full-Sky H α template map (Dickinson, Davies & Davis 2003; Finkbeiner 2003) to assess the level of free–free emission and the power-law spectrum associated with the synchrotron emission. Such information will be useful for comparison with the component separation that will be obtained from the SED analysis. The H α map was retrieved from the LAMBDA[5] database. For the SED analyses we will use the SMICA-CMB map retrieved from the PLA to directly remove the CMB component at the map level.

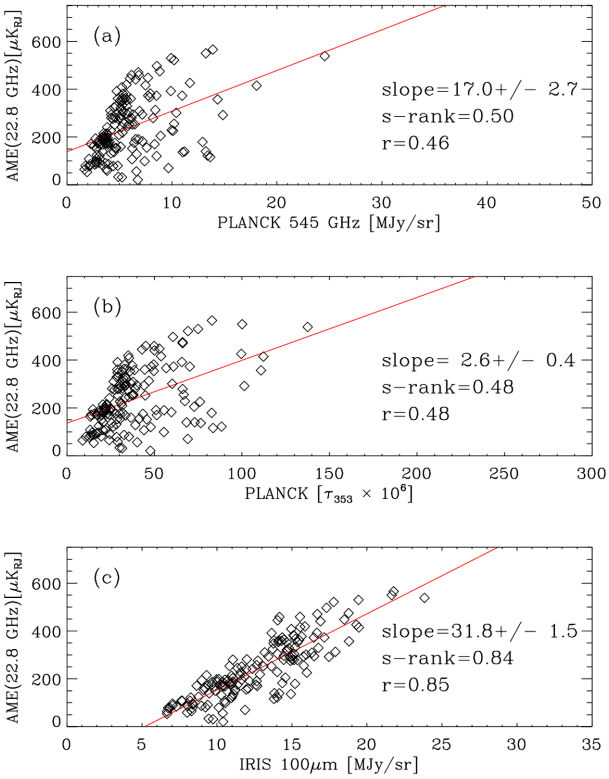

Figure 4. TT-plots of the Commander AME intensity towards the TMC region (delineated in white in Fig. 1) at 22.8 GHz with thermal dust amplitude at 545 GHz (a), the optical depth at 353 GHz, τ_{353} (b), and the IRAS map at 100 μm (c) from 1° resolution maps at $N_{\rm side} = 64$, where the sources displayed in Table 3 have been masked. The slopes are shown for comparison with the results provided by Planck Collaboration XXV (2016f) towards other molecular cloud regions. The Spearman rank correlation (*s*-rank) and Pearson correlation coefficient (*r*) are also shown. The best fit is shown as a red line.

4.1 Free–free components

Estimates of the free–free component towards the TMC complex can be assessed following the method proposed by Dickinson et al. (2003) (see also Planck Collaboration XXV 2016f). The temperature of the free–free component is given by

$$\frac{T_{\rm b}^{\rm ff}}{I_{\rm H\alpha}} = 1512 T_4^{0.517} 10^{0.029/T_4} \nu_{\rm GHz}^{-2.0} g_{\rm ff}, \quad (1)$$

where T_4 is the electron temperature in units of 10^4 K, $\nu_{\rm GHz}$ is the frequency in GHz, and $g_{\rm ff}$ is the Gaunt factor, which takes into account quantum mechanical effects. As noted in Planck Collaboration XXV (2016f) a pre-factor of 1.08 to account for the He II contribution that adds to the free–free continuum is included. In our calculations we also use the approximation to the Gaunt factor provided by Draine (2011) that is accurate to within about

[5]LAMBDA Data-Products, https://lambda.gsfc.nasa.gov/product/.

Downloaded from https://academic.oup.com/mnras/article-abstract/486/1/462/5255197 by CSIC user on 05 June 2020

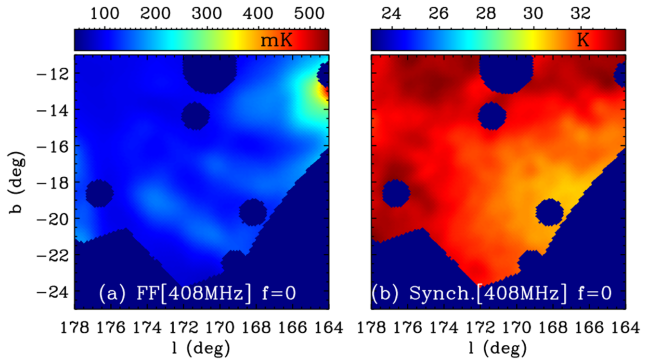

Figure 5. (a) Estimate of the free–free emission at 408 MHz obtained from the Hα emission map under the hypothesis that none of the Hα emission is absorbed by the thermal dust ($f = 0.0$). (b) Maps at 408 MHz of the synchrotron residual obtained after subtraction of the free–free component map shown on left, assuming a synchrotron power-law index of -2.80. All maps are 1° resolution HEALPIX maps at $N_{\rm side} = 512$.

1 per cent in the GHz frequency range at frequencies much higher than the 'plasma frequency', $\nu_{\rm P}$, of order a few MHz for a plasma with an electron temperature $T_{\rm e} \approx 7000$ K and electron density $n_{\rm e} \sim 10^{-2}$ cm^{-3}:

$$g_{\rm ff}(\nu, T_{\rm e}) = \ln\left\{\exp\left[5.960 - \frac{\sqrt{3}}{\pi}\ln(\nu_{\rm GHz} T_4^{-3/2})\right]\right\}. \quad (2)$$

To run the calculations we use the Full-Sky Hα template for microwave foreground prediction provided by Finkbeiner (2003) and the electron temperature, $T_{\rm e}$, template map from the Commander component separation analysis to give an almost uniform temperature $T_{\rm e} = 7000$ K over the whole area.

We first make the assumption that none of the Hα emission is absorbed by the dust (i.e. we assume a dust mixing factor $f = 0.0$). The map showing our results is shown in Fig. 5. At 408 MHz the free–free brightness temperature estimates obtained towards the TMC region are very low, with values showing variations below 200 mK and representing only $\sim$1 per cent of the 408 MHz total intensity map. Once the calculations are repeated for a central frequency of 13 GHz (see Fig. 6, panel a) the free–free brightness temperature estimates obtained towards the TMC region show variations lower than 0.10 mK, i.e. about 5–8 times lower than the free–free component obtained from the Commander analysis as shown in Fig. 3, panel b.

In order to take into account the possibility that a fraction of the Hα emission is absorbed by thermal dust emission we refer to Dickinson et al. (2003) and Harper, Dickinson & Cleary (2015). The expected emission $I_{\rm em}$ is related to the observed emission $I_{\rm obs}$ by the Hα absorption model:

$$I_{\rm obs} = \frac{I_{\rm em}}{\tau}\int_0^{f_\tau} {\rm e}^{\tau' - \tau}\,{\rm d}\tau' + (1 - f_\tau) I_{\rm em}. \quad (3)$$

This model assumes that a fraction, f_τ, of the H II gas and dust are mixed and in thermal equilibrium, and that the remaining fraction of the H II gas lies in front of the TMC thermal dust such that its Hα emission is unabsorbed. The Hα optical depth, τ, is related to the Hα absorption by $\tau = A({\rm H}\alpha)/(2.5\log_{10}(e))$, where $A({\rm H}\alpha) = 0.81{\rm Av}$. Very accurate column density and extinction maps of the TMC have been provided by the 2MASS survey from analysis of NIR colour excesses (see Lombardi, Lada & Alves 2010; Pineda et al. 2010). Because of limits inherent to the technique these maps tend to underestimate the extinction towards high

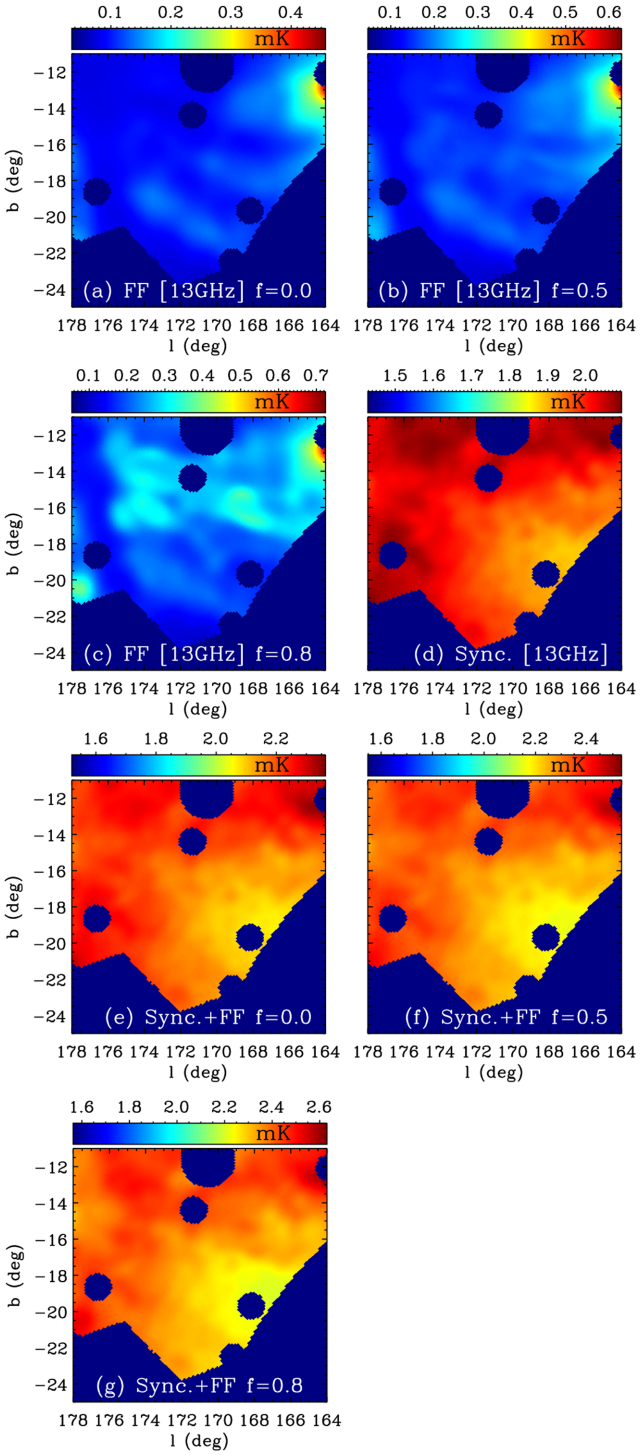

Figure 6. All maps are 1°-resolution HEALPIX maps at $N_{\rm side} = 512$. (a) Free–free map at 13 GHz, estimated from the Hα emission map under the hypothesis that none of the Hα emission is absorbed by the thermal dust ($f = 0.0$); (b) 13 GHz free–free map assuming a dust mixing factor $f = 0.5$; (c) 13 GHz free–free map assuming a dust mixing factor $f = 0.8$; (d) synchrotron map at 13 GHz assuming a synchrotron power-law index of -2.80; (e) coadded estimated maps of the synchrotron and free–free components at 13 GHz assuming none of the Hα emission is absorbed by the thermal dust ($f = 0.0$); (f) same as panel e but assuming a dust mixing factor $f = 0.5$; and (g) same as panel e but assuming a dust mixing factor $f = 0.8$.

Downloaded from https://academic.oup.com/mnras/article-abstract/486/1/462/5255197 by CSIC user on 05 June 2020

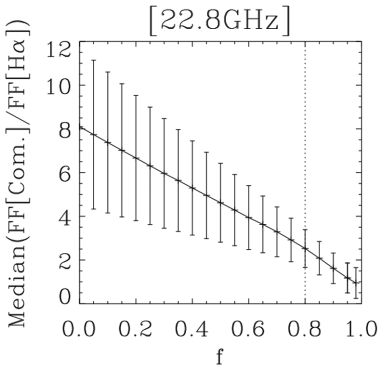

Figure 7. Variations of the median of the 22.8 GHz free–free ratio maps (free–free Commander map / H α calculated free–free maps) as a function of the dust mixing factor *f*. The standard deviations of the free–free ratio maps are superimposed on the median values and illustrate the amount of spatial variation between the pairs of maps. The dispersion between the ratio of the maps derived by each method is minimized and about uniform for dust mixing factors $\geq$0.8. The limit $f = 0.8$ is shown by the dashed vertical line.

column densities (see Planck Collaboration XXV 2011b; Planck Collaboration XI 2014c), which are regions we are interested by. In addition, these maps do not fully cover the region we are studying; therefore, in the following we use the PLA thermal dust optical depth at 353 GHz, τ_{353}, to estimate visible extinctions towards the TMC. Assuming that the column density and thermal dust optical depth at 353 GHz are proportional and related by $N_{\rm H} = 1.6 \times 10^{26} \tau_{353}$ (Planck Collaboration XIX 2016e), and that the extinction, $E(B-V)$, is such that $N_{\rm H}/E(B-V) \approx 6.94 \times 10^{21}$ cm^{-2} (Planck Collaboration XI 2014c), we have, $A({\rm H}\,\alpha) \approx 18674.4 \times R(V) \times \tau_{353}$, where the reddening parameter, $R(V)$, is expected to lie in the range of magnitudes [3.5, 5.5] (Vrba & Rydgren 1984, 1985). The 13 GHz maps obtained by considering an averaged value $R(V) = 4$ mag towards the TMC are shown in Fig. 6 for dust mixing fractions $f = 0.5$ and $f = 0.8$. The level of free–free intensity increases non-linearly with the dust mixing fraction, *f*, up to a factor 4 towards the highest column density regions of the TMC for a dust mixing factor, $f = 0.8$. We also note that the structure of the free–free emission looks more similar to that obtained by Commander when considering a dust mixing factor $f \approx 0.8$ than when considering lower values for *f* since the effect of high dust mixing fractions reveals the TMC morphology seen in the thermal dust maps. In Section 3.2 we show that at a central frequency of 22.8 GHz the Commander component separation returns self-consistent results towards the TMC region. In order to quantify how the morphology of the 22.8 GHz Commander free–free map compares with the morphology of the H α estimated free–free maps we made maps of the ratio between the two sets of maps obtained for different values of *f*. We then calculated the median values and the standard deviations of the set of maps. The results are shown in Fig. 7. One can see that the median of the ratio of the two maps is almost always >1 and decreases with *f*, and that the dispersion of the ratio is minimized and uniform for values of $f \geq 0.8$. Our calculations of the free–free maps with the Hα template rely on quite a simple extinction model and also assumes a uniform dust mixing factor over a large area. In addition, the Commander separation free–free map is expected to be subject to cross-talk with other physical components (AME, synchrotron). All in all though, the morphology structure of the maps start to be similar for values of $f \geq 08$ (as is also observed at a frequency of 13 GHz, see Fig. 3, panel b and 6, panel c). Keeping in mind all these caveats, in the following we will be conservative and consider a dust mixing factor $f \approx 0.8$, i.e. that about 80 per cent of the thermal dust is mixed with the H α gas.

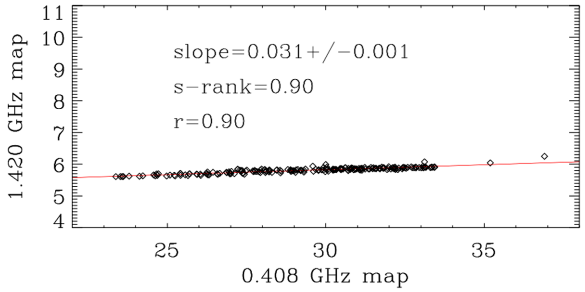

Figure 8. Correlation plot between the emission temperatures at 0.408 and 1.420 GHz towards the TMC (region delineated in white in Fig. 1) from 1° resolution HEALPIX maps at $N_{\rm side} = 64$. The uncertainties, assumed to be of the order of 10 per cent, are not shown for clarity.

4.2 Synchrotron frequency spectrum

The free–free component towards the Taurus region shows a very low intensity with respect to the total intensities observed at 408 MHz and 1.420 GHz. Therefore, one should expect synchrotron emission to be the major mechanism to produce the intensity observed at these two frequencies. This point is supported by the level of synchrotron emission displayed in Fig. 5 after the contribution of the estimated free–free emission has been removed from the maps. One should therefore expect a constant ratio, *r*, between the pixels, *i*, of the two emission maps such that

$$r = \frac{T_2(i)}{T_1(i)} \times \left(\frac{\nu_2}{\nu_1}\right)^{\beta_{\rm synch}} \quad (4)$$

where $\beta_{\rm synch}$ is the synchrotron power spectrum index (Platania et al. 1998) in the range of frequencies considered.

We conduct a *T*–*T* plot analysis of the 408 MHz and 1.420 GHz maps in order to get estimates of the power-law index $\beta_{\rm synch}$. For the map at 1.420 GHz we consider a correction factor equal to 1.55 to correct for the effect of the near sidelobes of the beam. Fig. 8 shows the temperature distribution at the two frequencies against each other from the HEALPIX maps at $N_{\rm side} = 64$ covering the TMC region. One can see a very tight linear relation from the fit shown in red over the data. We repeated a similar analysis for different sub-regions of the large region displayed in Fig. 1. The values of the power-law index are given in Table 4 for different cases such that all the emission is assumed to be synchrotron and free–free emission, and for the case in which the free–free component estimated from the H α map for a dust mixing factor, $f = 0.8$, is removed from the maps.

As expected from the very low emission of the free–free compared to the synchrotron emission discussed above, we find similar values for the power-law index $\beta_{\rm synch}$ to within the uncertainties, with a tendency towards a flatter index when the free–free is not subtracted. Once the map was split into two regions, however, we found that the synchrotron power spectral index is higher in the half-area map closer to the Galactic plane than in the half-area map further from the Galactic plane. Within the uncertainties, though, the values of $\beta_{\rm synch}$ obtained from the two half-maps are consistent with each other, as well as with the value of $\beta_{\rm synch}$ obtained towards the whole area and towards the TMC region. This means that, to within the uncertainties, a single power law with a fixed $\beta_{\rm synch} \sim$

Downloaded from https://academic.oup.com/mnras/article-abstract/486/1/462/5255197 by CSIC user on 05 June 2020

−2.80 over the whole area should be sufficient to characterize the synchrotron contribution towards the TMC.

4.3 Total intensity emission

A method that can be used to do a component separation analysis of the various components in emission contributing to the total emission of the TMC is to perform an SED analysis. This method consists of calculating the total emission of a given source at each frequency. Once the SED has been calculated one can use modelling to assess the fraction of the total intensity associated with the different components (synchrotron, free–free, thermal dust, and AME) at all frequencies. SED modelling analysis has been widely used in the literature (e.g. Watson et al. 2005; Planck Collaboration XX 2011a; Planck Collaboration XV 2014a; Génova-Santos et al. 2015, 2017).

4.3.1 Intensity flux densities of the TMC and L1527

In order to estimate the fraction of the total intensity emission associated with the TMC that would be AME in nature we use aperture photometry. For this purpose the units are first converted from CMB thermodynamic units (K_{CMB}) to RJ units (K_{RJ}) at the central frequency, then the maps are converted to units of Jy pixel^{-1} using $S = 2kT_{RJ}\Omega\nu^2/c^2$, where Ω is the HEALPIX pixel solid angle. The pixels are then summed in the aperture covering the region of interest to obtain an integrated flux density. An estimate of the background is subtracted using a median estimator of pixels lying on the region defined as the background region. The regions we integrate the signal over are shown in Fig. 9. The TMC is the area inside the contour line defined by isolating all pixels such that $A_V >$ 4.5 mag by using the A_V template from the *Planck* Legacy Archive (PLA). The L1527 dark cloud nebula is centred at position $(l, b) = (174.0^\circ, -13.7^\circ)$ in the TMC. The bulk of thermal dust emission seen at this location in the 353 GHz map over an area of about 3 deg^2 is also shown in the PLA A_V template map displayed in Fig. 9. This region was isolated by taking all the pixels such that $A_V > 10$ mag around the central position of L1527 in the PLA template. The median values are calculated from the background region (see Fig. 9) defined by isolating all pixels such that $A_V <$ 4.5 mag. Details on some tests conducted to assess whether the choice of the background region is relevant for our study are given in Appendix B.

For the TMC the SEDs obtained with the masks discussed above can be seen in Fig. 10, where the QUIJOTE points are shown in red, the *WMAP* points in green, the *Planck* points in blue, and the DIRBE points in yellow. The low-frequency points are shown in pale blue. The intensity flux densities are listed in Table 5 along with the intensity flux densities obtained towards the L1527 dark nebula, and are plotted as a function of frequency in Fig. 11. At first sight one can see that the low-frequency fluxes are very low in the SED of the TMC, whereas for L1527 the low-frequency points suggest clear positive component detections. In both SEDs a peak in the frequency range 10–60 GHz that should be associated with an AME component is clearly seen.

4.3.2 Intensity SED modelling

As discussed previously, the CMB component was removed from several maps by using the SMICA-CMB maps. This was done on all the maps between 10 and 353 GHz. The contamination level of the CMB is then fully negligible to within the uncertainties at frequencies higher than 70 GHz but had to be taken into account at lower frequencies. Therefore, we consider a total of four components (synchrotron, free–free, AME, and thermal dust) to model the intensity SED from a multicomponent fit. Following our conclusions concerning the assessment of the background region (see Appendix B), we assume that the AME associated with the molecular cloud material can be modelled with a single component of spinning dust (Draine & Lazarian 1998). For this we use the Bonaldi et al. (2007) model, a phenomenological model consisting of a parabola in logarithmic space [log(S_ν)–log(ν)]. The model is described by three free parameters: the slope at a frequency of 60 GHz, m_{60}, which is a function of the width of the parabola, the central frequency, $\nu_{\rm AME,peak}$, and the amplitude of the parabola, $S_{\rm AME,peak}$. The other components are modelled as follows: the synchrotron component is fitted by a single power law of index assumed to be constant, $\alpha_{\rm synch,int}$, and by the intensity of the synchrotron at a frequency of 1 GHz, $S_{\rm synch,\,1\,GHz}$. The free–free spectrum shape is fixed using equations 2–5 of Planck Collaboration XX (2011a). Our best guess for the electron temperature is the median value of the Commander template with, $T_e \simeq 7000$ K. The only remaining free parameter associated with the free–free component is the free–free amplitude, which can be parametrized by the effective EM. The thermal dust emission component is modelled by a single-component modified blackbody relation of the form, $\tau_{250}(\nu/1200\,{\rm GHz})^{\beta_{\rm dust}} B_\nu(T_{\rm dust})$, where τ_{250} is the averaged dust optical depth at 250 μm, $\beta_{\rm dust}$ is the averaged thermal dust emissivity and, $T_{\rm dust}$ is the thermal dust averaged temperature. The fit procedure includes priors on some of the parameters and consists of a minimization process using non-linear least-squares fitting in Interactive Data Language (IDL) with MPFIT (Markwardt 2009).

For the TMC the output parameters from the four multicomponent fits shown in Fig. 10 are listed in Table 6, top. They show quite a low free–free component, which is dominated by the AME component at the frequencies of the MFI. The averaged thermal dust temperature and spectral dust emissivity associated with the Taurus cloud region are found to be in the lower range of parameter values discussed by Planck Collaboration XXV (2011b), which indicates that the background region should be removing the warmer thermal dust grain components and isolating the thermal dust components at higher densities inside the TMC. On the other hand the synchrotron total flux is found to be very low at 1 GHz and consistent with no detection to within the uncertainties, still a low emission component could remain in the maps. This happens because the emission of the synchrotron in the region defined to estimate the background contribution almost dominates the total emission of the synchrotron component towards the TMC (see Fig. 5).

For L1527 the estimates of the four components from the multicomponent fit in intensity are given in Table 6 (top). The thermal dust temperature and thermal dust emissivity in L1527 and the TMC are similar to within the uncertainties, but the optical depth at 250 μm is found, on average, to be lower in L1527 than towards the TMC. For the TMC the area includes the regions such that A_V > 4.5 mag and therefore also all the regions such that $A_V > 10$ mag while the area of L1527 covers a smaller patch of the sky such that $A_V > 10$ mag. In addition, at the fit level, there is room left for degeneracy between the averaged value of $\beta_{\rm dust}$ and τ_{250}, and we expect this effect to be higher when integrating and fitting a grey body over a larger area. All these elements put together we think this is why the averaged value of τ_{250} over the whole TMC is about a factor 4 higher than towards L1527 alone. The averaged values of the thermal dust parameters from the fits displayed in Table 6

Downloaded from https://academic.oup.com/mnras/article-abstract/486/1/462/5255197 by CSIC user on 05 June 2020

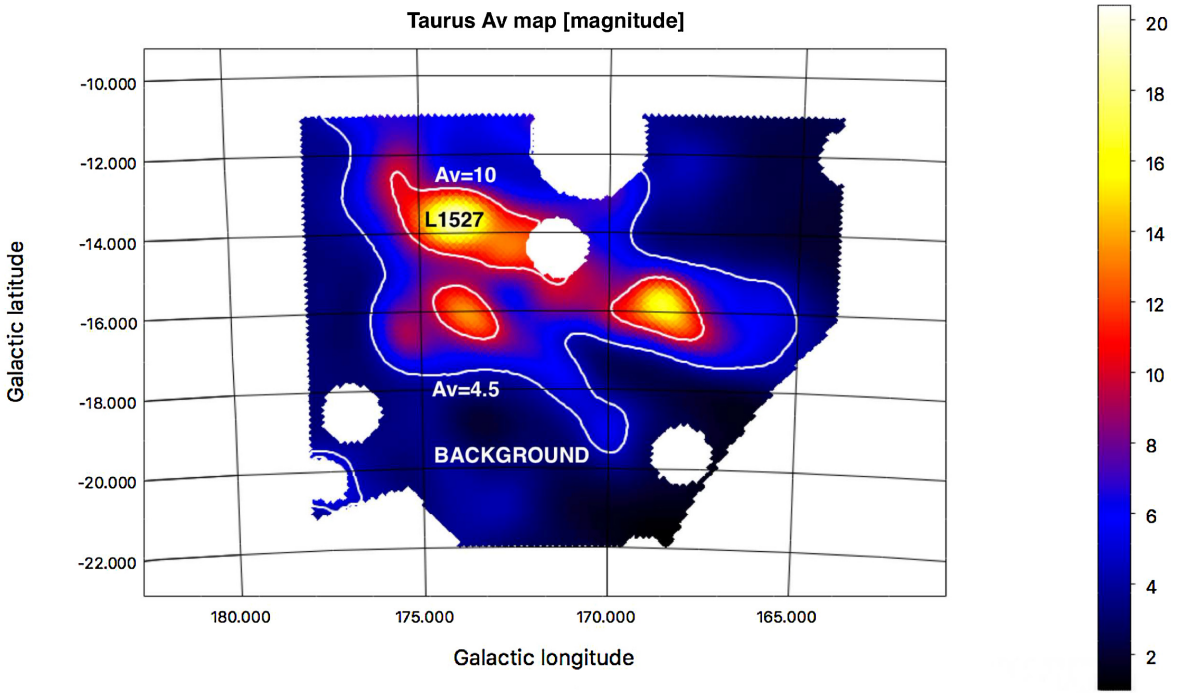

Figure 9. TMC region defined by isolating all pixels such that $A_V > 4.5$ mag (lowest contour). The region used to define the background is the region such that $A_V < 4.5$ mag. The L1527 region is defined by isolating all pixels such that $A_V > 10$ mag as shown by the contour plot (highest contour) centred on position $(l, b) = (174°, -13.5°)$.

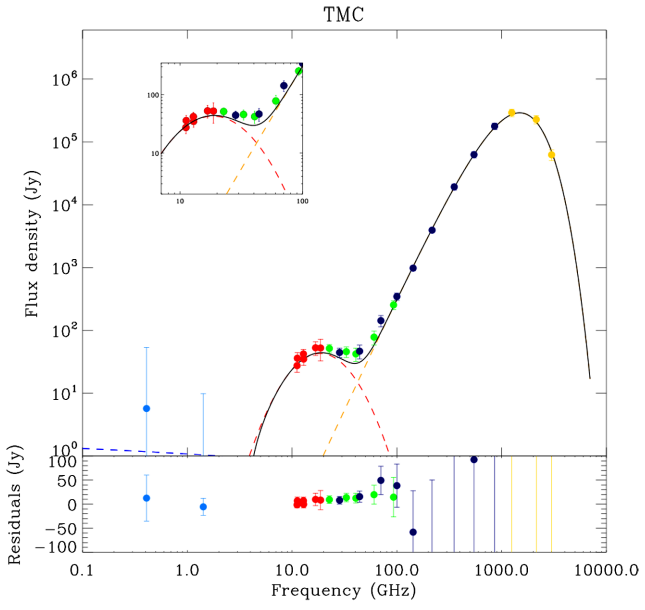

Figure 10. SED of the TMC region as defined in Fig. 9. The QUIJOTE intensity flux densities are shown with red filled circles, and the *WMAP*, *Planck*, and DIRBE intensity flux densities are shown with green, blue, and yellow filled circles, respectively. The low-frequency points are shown in pale blue. The result of the multicomponent fit is illustrated by the continuous black curve. The fit to the AME component is shown with the dashed red line. The fit to the free–free component is shown with the dashed blue line.

should be considered as indicative values only and one interested in details towards some specific areas of the TMC should for example refer to the *Planck* templates of thermal dust. The free–free components show an effective *EM* of the same order as that towards the TMC but is better constrained, which now also allows the fitting procedure to constrain the synchrotron component parameters with clear detection. This analysis also reconciles the variations of the synchrotron as a function of frequency since the power-law indices in temperature $\beta_{\rm synch} = -2.80 \pm 0.26$, and in flux $\alpha_{\rm synch,int} = -0.56 \pm 0.32$, are such that $\beta_{\rm synch} - 2 = \alpha_{\rm synch,\,int}$ to within the uncertainties. The total flux of the AME component is found to be about 3–4 times smaller than in the TMC, but a clear detection is still obtained thanks to the data provided by the QUIJOTE maps.

4.4 Limits on the level of linear polarization

4.4.1 Polarization maps of the TMC

The structures of the magnetic field pervading the TMC have been well studied from visible wavelengths to radio frequencies (e.g. Arce et al. 1998; Wolleben & Reich 2004; Chapman et al. 2011; Planck Collaboration XXXV 2016a). To get insight into these structures we first show in Fig. 12 the polarization maps of the TMC at 1.420 GHz (top row, left), 11 GHz (top row, middle), 13 GHz (top row, right), 22.7 GHz (bottom row, left), 30 GHz (bottom row, middle), and 353 GHz (bottom row, right). The polarization angles are all displayed following the cosmological convention (polarization angles counted positively clockwise from north to west in Galactic coordinates, see Górski et al. 2005). A comparison of the maps at 1.420, 11, and 353 GHz shows very similar and uniform polarization patterns over a large fraction of the area of the TMC. This can be seen in the histogram in panels a, b, and f in Fig. 13. In

Downloaded from https://academic.oup.com/mnras/article-abstract/486/1/462/5255197 by CSIC user on 05 June 2020

Table 5. Intensity flux densities in each frequency of the TMC and L1527 regions for the areas in Fig. 9, respectively. The values are shown with filled circles on the SED plot in Fig. 10 for the TMC and in Fig. 11 for L1527.

Frequency (GHz)	TMC fluxes (Jy)	TMC background (Jy)	L1527 fluxes (Jy)	L1527 background (Jy)	Calibration error (%)	Survey
0.4	5.7 ± 47.8	2277.4	16.2 ± 11.5	244.6	10	JB/Eff/Parkes
1.4	−7.9 ± 17.7	5404.0	7.5 ± 4.3	580.5	10	Stockert/Villa-Elisa
11.2[a]	27.5 ± 6.0	−27.8	7.4 ± 1.4	−3.0	5	QUIJOTE-MFI
11.2[b]	36.1 ± 8.2	−10.7	9.2 ± 1.9	−1.2	5	QUIJOTE-MFI
12.8[a]	42.2 ± 7.7	−17.7	11.3 ± 1.9	−1.9	5	QUIJOTE-MFI
12.9[b]	34.9 ± 7.2	−30.1	8.6 ± 1.7	−3.2	5	QUIJOTE-MFI
16.7[c]	52.9 ± 13.0	−0.4	8.9 ± 3.1	0.0	5	QUIJOTE-MFI
18.7[c]	52.5 ± 19.9	−10.8	9.9 ± 4.7	−1.2	5	QUIJOTE-MFI
22.7	51.6 ± 7.8	129.8	13.1 ± 1.9	13.9	3.2	*WMAP*
28.4	44.5 ± 7.7	108.4	11.9 ± 1.9	11.6	3.4	*Planck*
32.9	45.9 ± 8.8	100.2	10.1 ± 2.1	10.8	3.2	*WMAP*
40.6	42.3 ± 10.1	90.3	11.3 ± 2.4	9.7	3.2	*WMAP*
44.1	46.7 ± 11.6	97.1	12.4 ± 2.8	10.4	3.4	*Planck*
60.5	78.2 ± 19.6	93.3	19.8 ± 4.7	10.0	3.2	*WMAP*
70.4	143.1 ± 29.4	122.0	24.5 ± 6.9	13.1	3.4	*Planck*
93.0	254.3 ± 41.0	248.8	62.1 ± 9.8	26.7	3.2	*WMAP*
100.0	346.2 ± 45.1	352.7	85.9 ± 10.8	37.9	3.4	*Planck*
143.0	980.5 ± 86.3	1036.6	241.7 ± 20.6	111.3	3.4	*Planck*
217.0	(3.94 ± 0.24) × 10^3	4.57 × 10^3	970.3 ± 57.3	490.9	3.4	*Planck*
353.0	(1.92 ± 0.21) × 10^4	2.12 × 10^4	(4.67 ± 0.51) × 10^3	2.27 × 10^3	10.0	*Planck*
545.0	(6.28 ± 0.70) × 10^4	6.88 × 10^4	(1.54 ± 0.17) × 10^3	7.39 × 10^3	10.0	*Planck*
857.0	(1.78 ± 0.20) × 10^5	1.92 × 10^5	(4.35 ± 0.49) × 10^4	2.07 × 10^4	10.0	*Planck*
1249.1	(2.92 ± 0.40) × 10^5	3.45 × 10^5	(7.16 ± 0.96) × 10^4	3.71 × 10^4	11.9	COBE-DIRBE
2141.4	(2.27 ± 0.35) × 10^5	3.77 × 10^5	(5.61 ± 0.84) × 10^4	4.05 × 10^4	11.9	*COBE*-DIRBE
2997.9	(6.24 ± 0.12) × 10^5	1.64 × 10^5	(1.59 ± 0.29) × 10^4	1.77 × 10^4	11.9	*COBE*-DIRBE

Notes. [a]Horn 1.
[b]Horn 3.
[c]Horn 2.

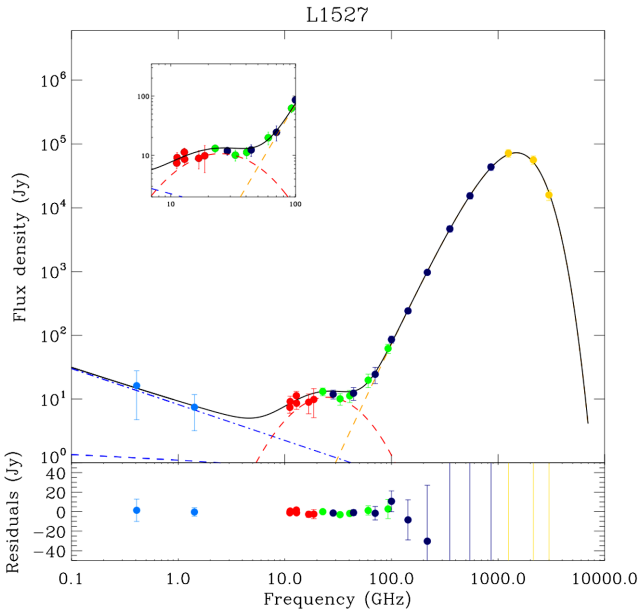

Figure 11. SED of the L1527 dark cloud as defined in Fig. 9. The filled circles colour code is the same as in Fig. 10. The fit to the AME component is shown with the dashed red line. The fit to the free–free component is shown with the dashed blue line, and the fit to the synchrotron component is shown with the point-dashed blue line.

Table 6. TMC and L1527 SEDs multicomponent output fit parameters in intensity (top table) and polarization (bottom tables).

	TMC	L1527
SED in intensity	Output fit parameters	Output fit parameters
EM (cm^{-6} pc)	9.9 ± 31.7	10.1 ± 6.0
$S_{\rm FF,1\,GHz}$ (Jy)	1.1 ± 3.5	1.1 ± 0.7
$S_{\rm synch,1\,GHz}$ (Jy)	−4.2 ± 12.0	8.2 ± 2.6
$\alpha_{\rm synch,\,int}$	−0.71 ± 3.42	−0.56 ± 0.32
m_{60}	3.6 ± 5.0	1.7 ± 2.7
$\nu_{\rm AME,peak}$ (GHz)	18.7 ± 7.1	25.4 ± 18.5
$S_{\rm AME,peak}$ (Jy)	43.0 ± 7.9	10.7 ± 2.7
$T_{\rm dust}$ (K)	15.6 ± 0.4	15.5 ± 0.4
$\beta_{\rm dust}$ (K)	1.61 ± 0.05	1.64 ± 0.05
τ_{250} × 10^{-3}	4.2 ± 0.5	1.1 ± 0.1
$\chi^2_{\rm red}$	1.27	0.63
SED in polarization	Output fit parameters	Output fit parameters
$S_{\rm synch,1\,GHz}$ (Jy)	43.60 ± 14.46	4.25 ± 1.47
$\alpha_{\rm synch,pol}$	−1.13 ± 0.23	−1.02 ± 0.20
$\pi_{\rm dust}$ (%)	6.54 ± 1.49	7.73 ± 1.91
$\chi^2_{\rm red}$	1.36	0.72
γ_0 (°)	1.28 ± 0.05	1.31 ± 0.05
RM (rad m^{-2})	6.56 ± 1.04	5.92 ± 1.04
$\chi^2_{\rm red}$	0.52	1.55

Downloaded from https://academic.oup.com/mnras/article-abstract/486/1/462/5255197 by CSIC user on 05 June 2020

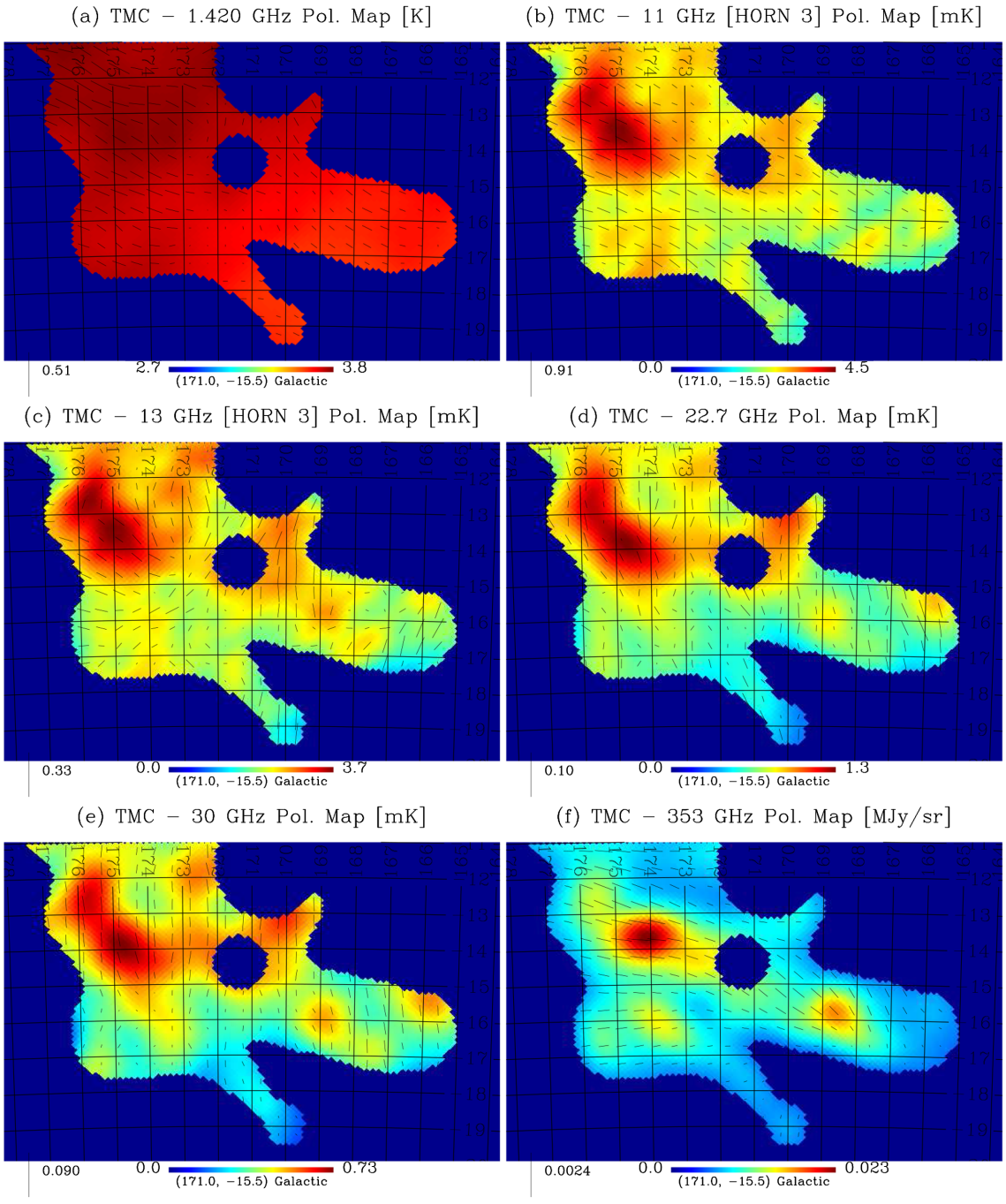

Figure 12. Polarization maps of the TMC with polarization pseudo-vector orientations overplotted. The polarization angles are all displayed following the cosmological convention (polarization angles counted positively clockwise from north to west in Galactic coordinates, see Górski et al. 2005). (a) 1.42 GHz polarization map. (b) QUIJOTE horn 3, 11 GHz polarization map. (c) QUIJOTE horn 3, 13 GHz polarization map. (d) *WMAP* 22.7 GHz polarization map. (e) *Planck* 30 GHz polarization map. (f) *Planck* thermal dust polarization map at 353 GHz.

these maps each pseudo-vector orientation should be perpendicular to the averaged magnetic field component projected on to the plane of the sky, $< \hat{B}_{\rm pos} >$. The data in the frequency range 1.420–10 GHz provide information about the magnetic fields producing polarized synchrotron since the free–free emission is expected to be unpolarized, whereas the data in the frequency range 60–3000 GHz probe the polarized emission of thermal dust. The data in the frequency range 10–60 GHz could provide combined information about the synchrotron, thermal dust, and AME component if this last component is polarized. The distribution of the polarization angles looks overall less uniform in the polarization maps at 13, 22.7, and 30 GHz, as can be seen with the broad distributions of the histogram in panels b, c, and d of Fig. 12. This could be due to averaging effects over some areas of the maps if the magnetic field orientations change over these areas, i.e. if Faraday depolarization occurs in the frequency range 10–40 GHz. This is not likely given the low level of free–free estimated in the TMC but Faraday depolarization has been studied at frequencies <2 GHz by

Downloaded from https://academic.oup.com/mnras/article-abstract/486/1/462/5255197 by CSIC user on 05 June 2020

Table 7. Median and standard deviations of the histograms of the polarization angles (P.A.) shown in Fig. 14. The calculations take into account that the P.A. distributions wrap on themselves modulo 180°.

Frequency (GHz)	TMC Median (P.A.) $\pm\,\sigma$ (P.A.) (°)	L1527 Median (P.A.) $\pm\,\sigma$ (P.A.) (°)
1.420	117.4 ± 25.1	123.6 ± 18.8
11	117.6 ± 16.1	119.4 ± 2.9
13	10.5 ± 44.8	160.8 ± 38.0
22.8	169.5 ± 15.3	1.5 ± 15.5
30	173.9 ± 31.7	164.6 ± 42.7
353	97.9 ± 29.6	101.7 ± 5.8

Wolleben & Reich (2004) in regions to the north of the TMC and was interpreted as produced by a Faraday screen at the boundaries of molecular clouds. Their analysis was possible because all their maps included absolute calibration. We do not have access to all their maps since only the 1.420 GHz map is publicly available. In addition, the baseline level of the QUIJOTE maps is not absolutely calibrated therefore we cannot directly repeat their analysis in the frequency range 10–40 GHz. A second explanation is that, in this frequency range, the AME component is polarized, which could produce perturbations in the polarization angle patterns. A third possibility is that some of the regions of the polarization maps are dominated by noise in the frequency range 10–30 GHz. A summary of the information provided by the polarization angle distributions is given in Table 7, where the median and standard deviations of the histograms shown in Fig. 13 are shown. In order to obtain further insights into whether the TMC is subject to Faraday depolarization or its polarization structure perturbed by the AME component and to decrease the impact of possibly noisy regions in the maps, in the following we conduct an analysis of the SEDs in polarization towards the TMC and L1527.

4.4.2 *Constraints on AME polarization in the TMC*

A further step to retrieve information about the various components is to calculate the polarized flux densities in the TMC. This is done by applying the same method as that used to estimate the flux densities in intensity. For this the fluxes of Q and U are first calculated using the same cloud and background regions as those used to calculate the fluxes in intensity (see Fig. 9). Since the values of Q and U can be positive or negative and P is not linear with Q and U, the calculation of $P = \sqrt{Q^2 + U^2}$ and $\pi = \sqrt{Q^2 + U^2}/I$ can be positively biased. Various methods to debias P exist in the literature, some of them taking into account priors on the distribution of P (e.g. Alina et al. 2016, and references therein). In the following we use Monte Carlo simulations. For this we take the quantities P, π, and γ and for each of these quantities we add a normal term drawn from a normal distribution with a width characteristic of the uncertainty on each quantity, repeat this process many times, and then measure the standard deviation with each quantity.

The debiased polarized flux densities $P^{\rm db}$, the fraction of polarization of the total intensity $\pi^{\rm db}$, and the polarization angle γ from the SED analysis are all plotted as a function of frequency in Fig. 14, from top to bottom respectively. All the values and their uncertainties are listed in Table 8. After the data are completely

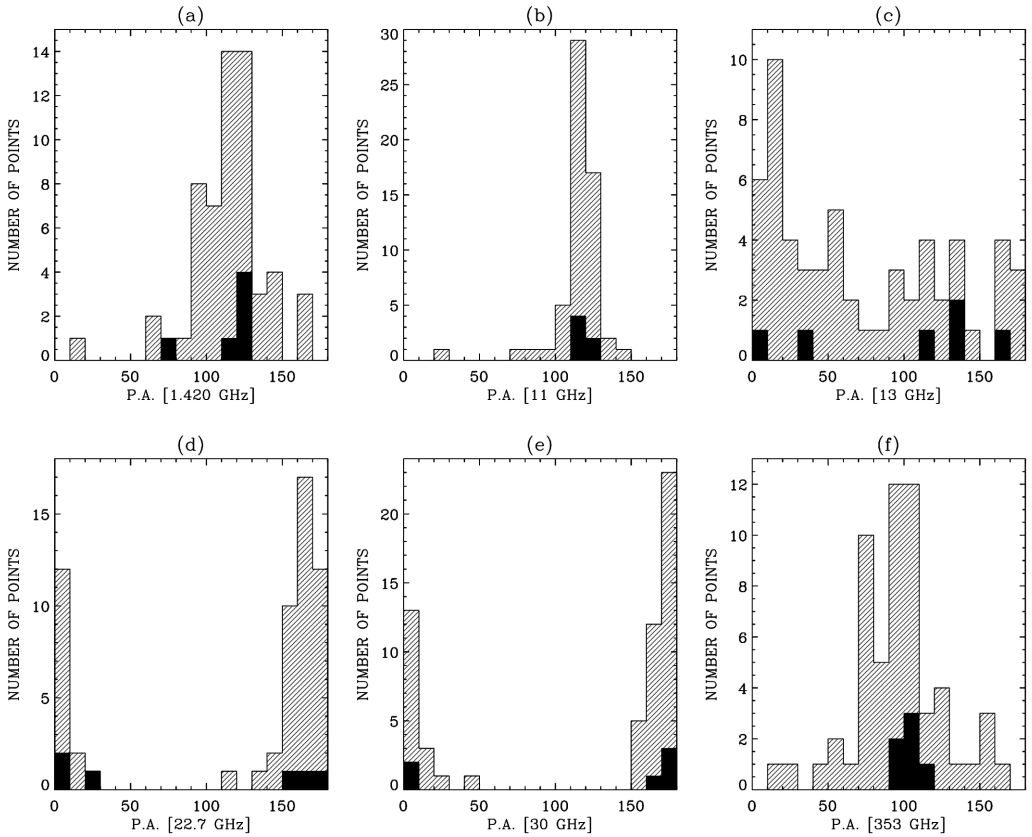

Figure 13. Histograms of the polarization angles shown in Fig. 12. The distribution of the polarization angles measured towards the TMC is shown in grey, and that associated with L1527 is shown in black.

Downloaded from https://academic.oup.com/mnras/article-abstract/486/1/462/5255197 by CSIC user on 05 June 2020

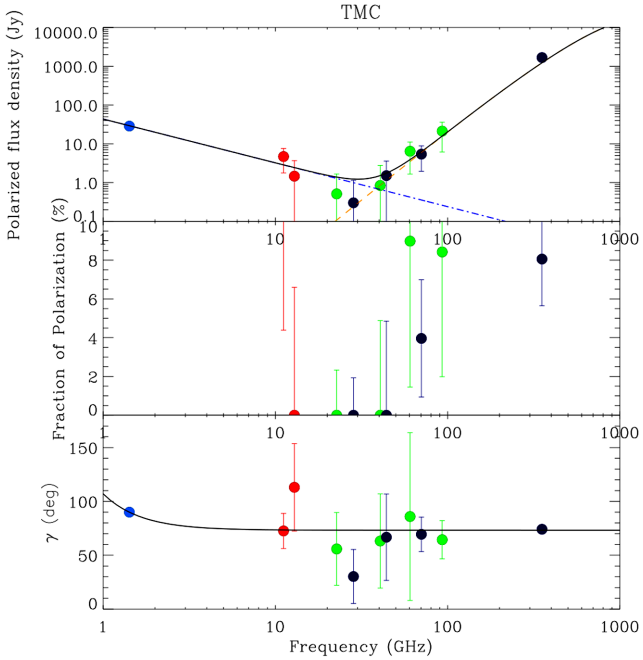

Figure 14. Top: Polarized flux density of the TMC region as defined in Fig. 9 plotted as a function of frequency. Middle: Fraction of polarization of the total intensity plotted as a function of frequency. Bottom: Polarization angles estimates plotted as a function of frequency. Fits to the data are shown with continuous dark lines (see text for details).

processed and debiased we note that in the MFI frequency range only data from horn 3 remain. The estimates of P and π from the data from horn 2 are dominated by their uncertainties and for that reason could not be debiased, therefore they are not included in the analysis.

Regarding the polarized synchrotron component one can see from Fig. 14 (top plot) that at 1.420 GHz the polarized flux is not at all consistent with zero ($\approx 35\sigma$ detection). A residual in the 1.420 GHz Q and U maps could come from the background subtraction dominating over the flux in the cloud region or vice versa. A closer look at the data shows that the background does not dominate the cloud region, and that therefore the polarized flux should be associated with the TMC. At 1.420 GHz the intensity flux is about -8 ± 18 Jy (Table 5), and the polarized flux density is 28.7 ± 0.8 Jy (Table 8). Within the uncertainties a total intensity flux that would be detected to 2σ would be of $\approx -8 + 2 \times 18 = 28$ Jy and about equal to the total polarized flux density (which would mean an approximately 100 per cent polarized synchrotron component). A detection of order 3σ would correspond to $\approx$46 Jy and imply that about 60 per cent of the synchrotron is polarized, assuming the free–free contribution is negligible as expected from the estimates shown in Fig. 5.

In order to get more insight into the synchrotron component we first assume that the SED in polarization shown at the top in Fig. 14 can be modelled by only two components: a polarized synchrotron component and a polarized thermal dust component of about similar polarization angle. The polarized synchrotron is fitted by a power law whose parameters can be compared to those of the power law obtained from the multicomponent fit in intensity. The thermal dust parameters from the thermal dust component fit in intensity are used as input parameters with an additional free parameter, $\pi_{\rm dust}$, the fraction of polarization of the thermal dust component, assumed to be constant in the frequency range 20–353 GHz. This hypothesis is driven by the shapes of the polarized flux density and fraction of polarization in both regions for frequencies higher than 60 GHz, taking into account the uncertainties. Some observational studies have shown that a flat polarization fraction spectrum can be expected in low and intermediate column density molecular cloud regions such as the TMC (Gandilo et al. 2016; Ashton et al. 2018), whereas high column density molecular cloud regions are not expected to show similar flat polarization spectra (see Vaillancourt & Matthews 2012). The output fit parameters are displayed at the bottom of Table 6. A fraction of polarization, $\pi_{\rm dust} = 6.54 \pm 1.49$ per cent, provides a good fit to the polarized component associated with the thermal dust. In the frequency range 1–20 GHz the polarized synchrotron is well fitted by a single power law of index $\alpha_{\rm synch,pol} = -1.13 \pm 0.23$. Such a power-law index in flux (equivalent to a power index ≈ -3.13 in brightness temperature) is steeper than the power-law indices in temperature estimated from the T–T plot analysis of the 0.408 and 1.420 GHz maps presented in Table 4. Assuming that the power-law indices in intensity and polarization are of the same order, this means that one should expect $\alpha_{\rm synch,pol} \approx -0.80$, which is not the case here. On a large scale towards regions north of the TMC complex Wolleben & Reich (2004) report from the analysis of observations at 1.408, 1.660, and 1.713 GHz that the diffuse synchrotron temperature component in polarization is well described by a power-law relation of index $\beta_{\rm synch} = -2.7$, a value not consistent with that obtained from the SED in polarization, but consistent to within the uncertainties with the values derived from our T–T plot analysis. On the other hand Faraday depolarization is also inferred from their analysis as due to Faraday screens with excessive rotation measures at the boundaries of molecular clouds (note that these results were not confirmed by Crutcher & Troland (2008) from their analysis of OH observations, which failed to detect the 20 μG magnetic field necessary to explain the strong Faraday rotations estimated by Wolleben & Reich 2004). In order to fit this effect we use the model $\gamma = \gamma_0 + RM \times \lambda^2$, where γ_0 is the polarization direction at $\lambda = 0$ ($\nu \rightarrow \infty$ in our case) and RM represents the rotation measure. The fit parameters are listed in Table 6 and show a rotation measure $RM = 6.56 \pm 1.04$ rad m^{-2} occurring at frequencies lower than the QUIJOTE frequencies. Our rotation measure is lower than those reported by Wolleben & Reich (2004) of order -18 to -30 rad m^{-2} and suggest this effect to be low in the TMC at the resolution of the observations.

Another possible scenario to account for the variations in the polarized intensity as a function of frequency would be to assume that, in addition to the thermal dust and the synchrotron components, the AME component is polarized. To test this possibility we show in Fig. 14 (middle) the variations of the fraction of polarization of the total intensity as a function of frequency. The total intensities used to calculate $\pi^{\rm db}$ are those from the SED in intensity. The flux density in intensity at 1.420 GHz is negative, which is why no fraction of polarization can be inferred at this frequency. In the frequency range 20–50 GHz the AME component peaks at a frequency $\nu_{\rm AME,peak} \approx 19$ GHz and the polarization fraction are consistent with zero, and only upper limits from the uncertainties can be derived on the maximum of polarization. The best data to put constraints on the level of polarization of the AME component comes from the point at 28.4 GHz. Assuming that the intensity and polarization components of the other components are negligible at this frequency, the data show that the fraction of AME polarization should be $\pi_{\rm AME} < 3.8$ per cent with 95 per cent confidence level (C.L.). Assuming now the extreme case in which the polarized fluxes Q and U at 28.4 GHz are produced only by the AME component,

Downloaded from https://academic.oup.com/mnras/article-abstract/486/1/462/5255197 by CSIC user on 05 June 2020

Table 8. Flux density estimates of Q (column 2) and U (column 3) for the TMC region as a function of the frequency (column 1). The quantities derived after debiasing are the polarized flux densities $P^{\rm db}$ (column 4), the fraction of polarization of the total intensity $\pi^{\rm db}$ (column 5), and the polarization angle γ (6). These last three quantities are plotted as a function of frequency in Fig. 14.

ν (GHz)	$Q \pm \sigma_Q$ (Jy)	$U \pm \sigma_U$ (Jy)	$P^{\rm db} \pm \sigma_{P^{\rm db}}$ (Jy)	$\pi^{\rm db} \pm \sigma_{\pi^{\rm db}}$ (%)	$\gamma \pm \sigma_\gamma$ (°)
1.4	− 28.37 ± 1.28	− 0.02 ± 0.01	28.66 ± 0.77	− ± −	90 ± 1
11.2	− 4.10 ± 1.73	− 2.85 ± 1.17	4.70 ± 2.91	17.87 ± 13.48	73 ± 16
12.9	− 1.42 ± 1.36	1.48 ± 1.06	1.46 ± 2.23	0.00 ± 6.60	113 ± 41
22.7	− 0.38 ± 0.73	− 0.97 ± 0.65	0.48 ± 1.16	0.00 ± 2.34	56 ± 34
28.4	0.37 ± 0.56	− 0.65 ± 0.45	0.26 ± 0.84	0.00 ± 1.92	30 ± 25
40.6	− 1.01 ± 1.11	− 1.37 ± 1.13	0.82 ± 1.93	0.00 ± 4.87	63 ± 44
44.1	− 1.34 ± 1.05	− 1.41 ± 1.00	1.50 ± 2.08	0.00 ± 4.85	67 ± 40
60.5	− 6.77 ± 2.00	− 0.97 ± 2.45	6.62 ± 4.77	8.95 ± 7.50	86 ± 78
70.4	− 4.39 ± 1.85	− 3.83 ± 1.57	5.38 ± 3.45	4.00 ± 3.03	69 ± 16
93.0	− 13.62 ± 6.60	− 16.95 ± 7.34	21.12 ± 15.11	8.29 ± 6.45	64 ± 18
353.0	− 1302.55 ± 196.99	− 807.09 ± 123.46	1679.52 ± 347.92	8.08 ± 2.41	74 ± 3

and in which only the intensity of the AME component is used to calculate the fraction of polarization (i.e. $I_{\rm AME} \approx I_{\rm total} - I_{\rm TD}$ since from the fit $I_{\rm Sync} \approx 0$ whether the synchrotron is assumed to be 0 per cent or 100 per cent polarized at 28.4 GHz), a simple cross product gives a little less stringent constraint with a higher upper limit of 4.2 per cent (95 per centC.L.).

Finally we show in the bottom plot in Fig. 14 the distribution of the polarization angles associated with the TMC. One can see some variations with respect to the fit, in particular the polarization angle estimated at 28.4 GHz ($\gamma \sim 30°$) departs from the fit, as does the polarization angle at 12.9 GHz ($\gamma \sim 113°$), and the two angles are almost perpendicular to each other even though the uncertainties in both measurements are quite large. Polarized AME components could be the explanation but the large difference between the two angles could also be explained by dilution effects from the integration over a large area like the one covered by the TMC, or simply because some regions in each map are noise dominated. This second hypothesis may be more likely given the variations of the polarization angles observed in some of the polarization maps in Fig. 12. This can also be seen with the variations with frequency of the polarization angle dispersion values in Table 7.

4.4.3 Constraints on AME polarization in L1527

For comparison with the TMC, we conducted an analysis of the SED in polarization of L1527. The background region used to make the calculations is the same one as before. The flux densities in polarization are listed in Table 9 and plotted as a function of frequency in Fig. 15. Assuming a uniform fraction of thermal dust emission polarization in the frequency range 20–353 GHz we find a polarization fraction slightly higher than in the TMC, but the two estimates are consistent with each other within the uncertainties, in agreement with what one might expect from the level of polarization shown in the 353 GHz polarization map (see Fig. 12). The power-law index describing the polarized synchrotron variations with frequency ($\alpha_{\rm synch,pol} = -1.02 \pm 0.20$) now gives a consistent picture to within the uncertainties with the power-law indices from the intensity analysis in temperature and flux, and is in agreement with the value $\beta_{\rm synch,obs} = -2.7$ found by Wolleben & Reich (2004) from their analysis of the polarized temperatures in large scale in regions north of the TMC complex.

In order to check for possible Faraday screens that could produce Faraday depolarization towards L1527, and therefore a rotation of the polarization angles towards low frequencies, we repeated the fit analysis on the distribution of polarization angles. The results of the fit, $RM = 5.92 \pm 1.04$ rad m^{-2} and $\gamma_0 = 1.31° \pm 0.05°$, are very similar to the results obtained for the TMC, but the fit is slightly less constrained ($\chi^2_{\rm red} = 1.55$). The quality of the fit is lower for L1527 than for the TMC because the value of the polarization angles at frequencies 28.4 GHz and 40.6 GHz departs from the trend shown by the other angles at frequencies greater than 10 GHz. For comparison with the results obtained in the TMC, a look at the distribution of the polarization angles (see Fig. 12) displayed over the area covered by L1527 indeed shows overall uniform distributions of the pseudo-vectors at each frequency but with different orientations in the frequency range 10–50 GHz. The perturbation of the polarization angle values could come from AME components having different polarization orientations as a function of frequency but, all in all, the uncertainties in the polarization angles listed in Table 9 are still high and do not permit any firm conclusion.

Finally, as was discussed above for the TMC, here again we assume the best data to put constraints on the fraction of AME polarization are the those for 28.4 GHz. If none of the other components is polarized and of negligible intensity, we find an upper limit $\pi_{\rm AME} < 4.5$ per cent (95 per cent C.L.). On the other hand, if the other component intensities are not negligible and their modelled estimates are removed from the total intensity, and if the polarization is produced only by the AME component, a worse constraint $\pi_{\rm AME} < 5.3$ per cent (95 per cent C.L.) is obtained.

5 DISCUSSION

In our analysis we have shown that towards and around the TMC in the maps at frequencies 0.408 and 1.420 GHz the emission of the synchrotron component predominates over the free–free emission independently of the dust mixing fraction of the H α with the thermal dust grains. This result is shown at a frequency of 0.408 GHz in Fig. 5, where one can see that the emission of the free–free is expected to be only about 1 per cent or lower of the total emission of the maps. From a TT-plot analysis of the same two maps we have parametrized the variation of the synchrotron emission with

Downloaded from https://academic.oup.com/mnras/article-abstract/486/1/462/5255197 by CSIC user on 05 June 2020

Table 9. Flux density estimates of Q (column 2) and U (column 3), for the L1527 dark cloud as a function of the frequency (column 1). The quantities derived after debiasing are the polarized flux densities $P^{\rm db}$ (column 4), the fraction of polarization of the total intensity $\pi^{\rm db}$ (column 5), and the polarization angle γ (6). These last three quantities are plotted as a function of frequency in Fig. 15.

ν (GHz)	$Q \pm \sigma_Q$ (Jy)	$U \pm \sigma_U$ (Jy)	$P^{\rm db} \pm \sigma_{P^{\rm db}}$ (Jy)	$\pi^{\rm db} \pm \sigma_{\pi^{\rm db}}$ (%)	$\gamma \pm \sigma_\gamma$ (°)
1.4	−3.00 ± 0.30	−0.01 ± 0.00	3.03 ± 0.08	51.87 ± 41.40	80 ± 1
11.2	−0.50 ± 0.41	−0.47 ± 0.28	0.57 ± 0.70	0.00 ± 10.62	68 ± 34
28.4	0.19 ± 0.13	−0.09 ± 0.11	0.15 ± 0.23	0.00 ± 1.98	13 ± 21
32.9	−0.36 ± 0.20	−0.20 ± 0.23	0.33 ± 0.44	0.00 ± 4.74	75 ± 59
40.6	0.08 ± 0.27	−0.42 ± 0.27	0.24 ± 0.48	0.00 ± 4.36	39 ± 26
60.5	−1.10 ± 0.48	−0.35 ± 0.59	0.97 ± 1.15	5.18 ± 6.24	81 ± 70
70.4	−1.07 ± 0.44	−0.38 ± 0.37	1.03 ± 0.84	4.67 ± 4.43	80 ± 58
93.0	−2.48 ± 1.57	−3.66 ± 1.74	4.18 ± 3.66	6.52 ± 6.19	62 ± 22
353.0	−305.82 ± 46.56	−156.57 ± 27.16	376.61 ± 79.38	7.23 ± 2.20	76.44 ± 2.75

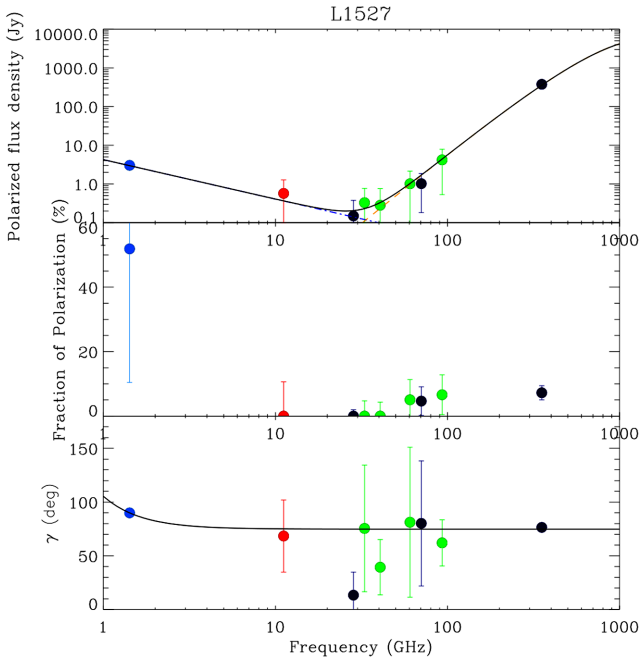

Figure 15. Top: Polarized flux density of the L1527 dark cloud as defined in Fig. 9 plotted as a function of frequency. Middle: Fraction of polarization of the total intensity plotted as a function of frequency. Bottom: Polarization angle estimates plotted as a function of frequency. Fits to the data are shown with continuous dark lines (see text for details).

frequency towards the TMC by a single power law of power-law index $\beta_{\rm synch} = 2.80 \pm 0.26$ (see Table 4). This result is consistent with that obtained by Wolleben & Reich (2004), who showed from the analysis of observations at 1.408, 1.660, and 1.713 GHz that the diffuse synchrotron temperature component in polarization is well described by a power-law relation of index $\beta_{\rm synch} \approx -2.7$.

In order to put constraints on the level of polarization of the AME component we have made an analysis of the SED in intensity (Fig. 10) and polarization (Fig. 14) of the TMC. The area of the TMC and the background regions defined and used for this are shown in Fig. 9. Thanks to the QUIJOTE data maps at 11, 13, 17, and 19 GHz the multifit component of the SED in intensity shows a clear detection of AME of total intensity $S_{\rm AME,peak} = 43.0 \pm 7.9$ Jy peaking at a central frequency of about 19 GHz (Table 6). A clear detection of a synchrotron component is not possible in the SED in intensity but a clear detection is seen in the SED in polarization, indicating that a synchrotron component is indeed associated with the TMC. From the analysis of the SED in polarization at a frequency of 28.4 GHz we have estimated an upper limit $\pi_{\rm AME} < 4.2$ per cent with 95 per cent confidence level (C.L.) (worst case scenario) and $\pi_{\rm AME} < 3.8$ per cent with (95 per cent C.L.) if the intensity of all the other components is negligible at this frequency.

A look at the polarization maps at 1.420 and 353 GHz (Fig. 12) shows very uniform polarization patterns that indicate the presence of uniform magnetic fields on a large scale towards the TMC (these were the main motivation for observing the TMC with the MFI). A look at the polarization maps in the frequency range 10–40 GHz, though, indicates variations of the polarization angles on smaller scales. These variations are also seen in the variation of the polarization angles γ estimated from the analysis of the SED in polarization (Fig. 14), but the uncertainties in the polarization angles are generally too large to make any strong conclusions (Table 8). In addition, such variations of the polarization angles on a smaller scale towards the TMC could result in reducing the net fraction of polarization estimated after integration over the total area of the TMC and thus mislead the interpretation of the constraints put on $\pi_{\rm AME}$ in the TMC. In order to address this problem and to understand what could be the origin of these variations of γ in the frequency range 10–50 GHz we repeated our analysis towards the L1527 dark cloud nebula. On the one hand the analysis of the SED in intensity (Fig. 11) gives a power-law description of the synchrotron component as a function of frequency consistent with that observed on a large scale (this work and Wolleben & Reich 2004). In addition, the overall trend of the distribution of the polarization angles in the frequency range at 1.42–353 GHz are very similar. This is confirmed by the fits to the distributions of polarization angles in the TMC and L1527 respectively. The *RM* obtained from the two fits are low and of order ∼6.6 rad m^{-2} in the TMC and ∼5.9 rad m^{-2} in L1527. For comparison Wolleben & Reich (2004) derived towards regions north of the TMC *RM* of −18 and −30 rad m^{-2} to model their observations at frequencies below 2 GHz. These results suggest that if there are Faraday screens towards the TMC and L1527 their effects are quite low at the resolution of the observations. On the other hand, the SED in polarization of L1527 (Fig. 15) confirms the

Downloaded from https://academic.oup.com/mnras/article-abstract/486/1/462/5255197 by CSIC user on 05 June 2020

trends observed in the variations of the polarization angles γ in the frequency range 10–50 GHz. Since these variations are not expected to come from Faraday depolarization, an alternative explanation is that another component is polarized in a direction different from the direction of the magnetic fields inferred from the polarization maps at 1.420 and 353 GHz, but the uncertainties in the estimates of such a component are too high to derive any strong conclusion. In any case, if this polarized component is emitted by the carriers at the origin of the AME we expect its level of polarization at 28.4 GHz in L1527 to be $\pi_{\rm AME} < 5.3$ per cent (95 per centC.L.), or $\pi_{\rm AME} < 4.5$ per cent (95 per centC.L.) if the intensities of all the other components are negligible at this frequency.

In Section 3 we discuss qualitatively how the 13 GHz MFI-QUIJOTE SMICA-CMB subtracted map compares morphologically with the map obtained by combining the Commander separation component templates (synchrotron, free–free, thermal dust, and AME) at a reference frequency of 13 GHz. As a further test we now discuss quantitatively how the Commander AME components compare to the AME component derived from the SED analysis in intensity. To do this we calculated the various template maps obtained by combining the two Commander AME templates at the reference frequencies of the observations in the range 10–65 GHz. We then calculated the intensity fluxes of the Commander AME by using the same masks as those used to calculate the SED in the TMC and L1527. We also calculated the total flux densities of the synchrotron, free–free, thermal dust, and AME components by combining the template maps of all the components and calculated the flux densities for each component. The results are shown in Fig. 16 for both regions. In the plots showing only the fits of the AME components the dark curves show the AME flux densities obtained with the Commander templates in the frequency range 10–65 GHz panels a and c. The red curves show the SEDs of the AME fit components obtained in this analysis. In both regions we find the AME flux densities estimated with each method (our component separation including the QUIJOTE-MFI data and the component separation with the Commander algorithm Planck Collaboration XXV 2016f) are similar within a factor two at frequencies higher than ∼25 GHz. On the other hand the lack of information in the frequency range 10–20 GHz clearly shows the AME components to be underestimated by the Commander method. Such results are understood as originating from cross talk between the synchrotron, free–free, and AME with the consequence of underestimating the AME intensities in the TMC and L1527 regions. A look at the flux densities of the other Commander components is shown in panels b and d, Fig. 16. The Commander AME density fluxes are shown with black dashed curves and triangle symbols. The Commander thermal dust flux densities are displayed with the green dashed double dotted lines with square symbols. The Commander synchrotron flux densities calculated by assuming a power law in temperature of index $\beta_{\rm synch} = -2.8$ are shown with dark blue dotted lines and plus symbols. The Commander free–free flux densities are shown with pale blue dotted lines and star symbols. A comparison of these plots with those in panels a and c indeed clearly shows that the AME Commander flux densities are underestimated at the cost of overestimating the Commander free–free flux densities in both regions since, in the particular case of the TMC complex, the Commander synchrotron component associated with the cloud structures is found to be very low. For that reason one can see that consistent fits to the total AME components are obtained at frequencies higher than ∼25 GHz by each method and divergence of the fits at frequencies lower than ∼25 GHz. This limit is shown in all the plots with a dashed vertical line centred at a frequency

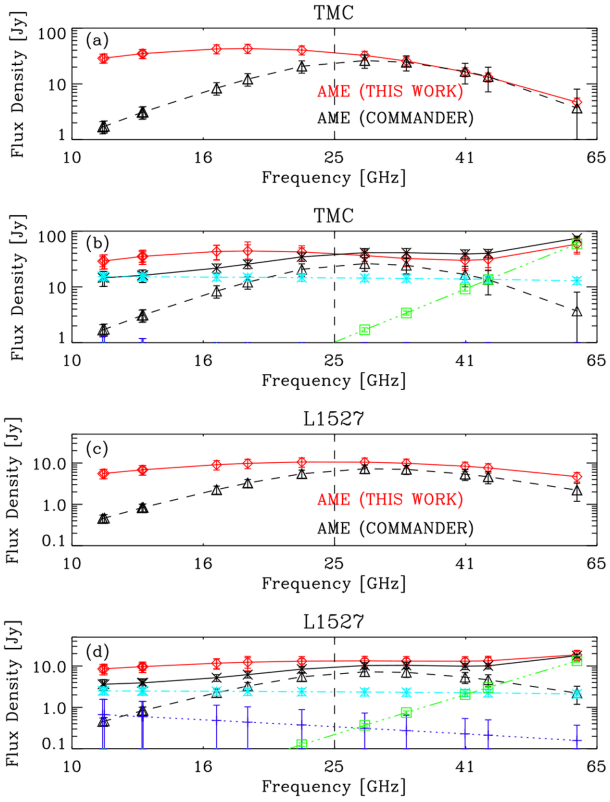

Figure 16. SEDs of the TMC and L1527 in the frequency range 10–65 GHz. Panels (a) and (c): AME flux densities from this analysis and from Commander. The dark curves show the SEDs of the total flux densities of the two AME components from Commander and the red curves show the SED of the AME from this analysis. Panels (b) and (d): the total flux densities obtained with our multifit components are shown with red curves and diamond symbols. The total flux densities obtained with Commander are shown with the black curves and star symbols. The Commander AME flux densities are shown with black dashed curves and triangle symbols. The Commander thermal dust flux densities are displayed with the green dashed double dotted lines with square symbols. The Commander synchrotron flux densities calculated by assuming a power law in temperature of index $\beta_{\rm synch} = -2.8$ are shown with dark blue dotted lines and plus symbols. The Commander free–free flux densities are shown with pale blue dotted lines and star symbols.

of 25.5 GHz for illustration. To summarize these results, the ratio of the flux densities of the total AME components obtained by each method are listed in Table 10. The high values of the ratios estimated in the frequency range 10–20 GHz clearly demonstrate the relevance and importance of the QUIJOTE-MFI data for sampling the electromagnetic spectrum at radio frequencies lower than 20 GHz. Without the QUIJOTE-MFI information, the Commander component separation methods underestimates the AME density fluxes. With the QUIJOTE-MFI data the location of the AME peaks and the width of the AME features can be characterized more accurately.

In Section 3.2 we discuss the similarity between the morphology of the Commander free–free map and the free–free map using the Hα map, and calculated, assuming a dust mixing fraction, $f = 0.8$. In order to quantify how the Hα free–free maps could reproduce the free–free SED profiles obtained from the multicomponent fit analysis of the SEDs in intensity we have calculated the SED spectra obtained in the TMC and in L1527 for various values of

Downloaded from https://academic.oup.com/mnras/article-abstract/486/1/462/5255197 by CSIC user on 05 June 2020

Table 10. Ratio between the AME intensity flux densities obtained in this work and those estimated with Commander for the TMC and L1527 as displayed in the plots shown in Fig. 16.

Frequency (GHz)	TMC $\frac{S(\text{Fit})}{S(\text{Commander})}$ (AME)	L1527 $\frac{S(\text{Fit})}{S(\text{Commander})}$ (AME)
11.2	17.0	12.3
11.2	16.7	12.1
12.8	11.3	8.3
12.9	11.2	8.2
16.7	5.0	4.0
18.7	3.5	3.0
22.7	2.0	1.9
28.4	1.2	1.5
32.9	1.1	1.4
40.6	1.0	1.6
44.1	1.0	1.6
60.5	1.3	2.1

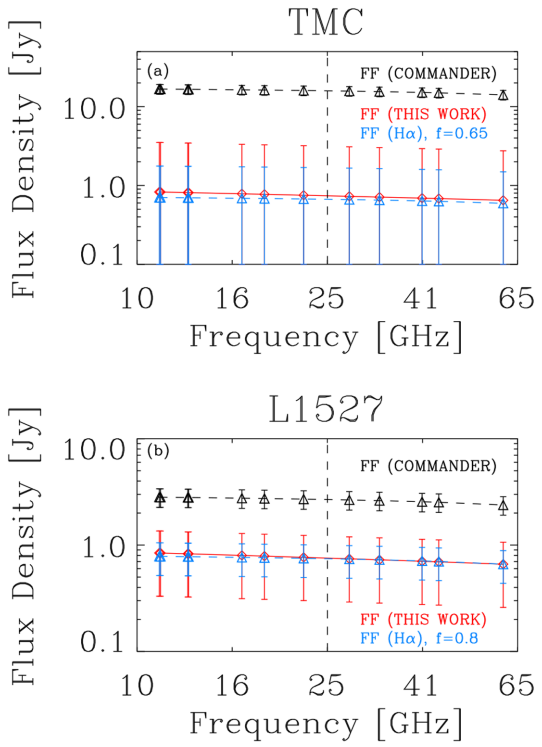

Figure 17. Free–free SEDs of the TMC (panel a) and L1527 (panel b) in the frequency range 10–65 GHz. In each panel, the free–free flux densities from this analysis are shown in red. The free–free flux densities from Commander are shown in black, and the free–free flux densities calculated with the H α map are shown in blue. The free–free flux densities obtained from our analysis can be reproduced assuming a spatially uniform dust mixing factor $f = 0.65$ for the whole TMC and a dust mixing factor $f = 0.8$ for L1527.

the dust mixing factor. Our best fits to the data are shown in Fig. 17. As discussed above, for each region the SED obtained with the Commander free–free map is overestimated with respect to our fits. On the other hand, the free–free flux densities obtained from our analysis can be reproduced assuming a spatially uniform dust mixing factor $f = 0.65$ for the whole TMC and a dust mixing factor $f = 0.8$ for L1527. We point out that for the TMC the consistency between our fit and the free–free H α calculated SED is quite sensitive to the tuning of the dust mixing fraction. We interpret this as an indication that the dust mixing fraction is not necessarily uniform over the whole TMC. The extinction model we use to estimate the Hα optical depth also assumes a linear relation with the thermal dust optical depth τ_{353}, but variations are expected towards high and low column density regions (Planck Collaboration XI 2014c). All in all, though, and despite the above caveats, the comparisons of our SED multicomponents fit analyses including new data from the QUIJOTE-MFI with the free–free maps calculated with the Hα maps give quite a consistent picture of the free–free component assuming an average dust mixing fraction $f \approx 0.80$. From this analysis we drive the conclusions that, towards the TMC and L1527, the Commander component separation method tends to overestimate the free–free component at the cost of underestimating the AME component.

6 CONCLUSIONS

We acquired new linear polarimetry observations of the TMC region observed in the frequency 10–20 GHz with the MFI mounted on the first telescope of the QUIJOTE experiment. The data were obtained over a total integration time of about 423 h towards an area of $\approx 17^\circ \times 17^\circ$ during 2015 March–July.

From the combination of the QUIJOTE data with the *WMAP* 9-yr data release, the *Planck* second data release, the DIRBE maps, and ancillary data we detect an AME component of total emission $S_{\text{AME,peak}} = 43.0 \pm 7.9$ Jy (5.4 σ detection) in the TMC and $S_{\text{AME,peak}} = 10.7 \pm 2.7$ Jy (4.0 σ detection) in L1527. In the TMC the AME peaks around a frequency of 19 GHz and around a frequency of 25 GHz in L1527. In the TMC, the analysis of the SED in polarization at the *Planck* channel of 28.4 GHz put constraints on the level of polarization of the AME with an upper limit $\pi_{\text{AME}} < 4.2$ per cent (95 per cent C.L.), and $\pi_{\text{AME}} < 3.8$ per cent (95 per cent C.L.) if the intensity of all the other components is negligible at this frequency. The same analysis in L1527 leads to $\pi_{\text{AME}} < 5.3$ per cent (95 per cent C.L.) or $\pi_{\text{AME}} < 4.5$ per cent (95 per cent C.L.) if the intensities of all the other components are negligible at this frequency.

From a comparison of the Commander free–free map with the free–free maps calculated with the Hα map for several dust mixing fraction, and from a comparison of the free–free flux densities obtained from our analysis including the QUIJOTE-MFI data with the Commander free–free flux densities and with the Hα free–free flux densities, we reach the conclusion that in the TMC and L1527 the dust gas mixing fraction should be of order 80 per cent.

In the TMC and L1527 the flux densities associated with the AME component are consistent to within a factor 2 with those obtained from the analysis of the Commander template maps at frequencies ≥ 22.7 GHz. On the other hand, because the Commander component separation products were produced without data in the frequency range 10–20 GHz we find that the flux densities of the AME are drastically underestimated by the Commander analysis in this frequency range, and that the Commander free–free flux densities are overestimated at all frequencies. Our analysis shows the importance of the QUIJOTE-MFI data to accurately separate the synchrotron, free–free, and AME components.

Further investigation including additional QUIJOTE data in the frequency range 10–42 GHz, as well as supplementary information provided by C-BASS 5 GHz data (e.g. King et al. 2014; Irfan et al. 2015), should be useful in confirming our analysis and constraining the polarization components observed in the frequency range 1–50 GHz in L1527 and the TMC.

Downloaded from https://academic.oup.com/mnras/article-abstract/486/1/462/5255197 by CSIC user on 05 June 2020

ACKNOWLEDGEMENTS

We thank J. P. Leahy for fruitful discussions about 3C 123. We thank Juan Uson and Wolfgang Reich for useful comments. We thank the anonymous referee whose comments helped to improve this work. We thank T.J. Mahoney for revising the English of the draft. FP acknowledges the European Commission under the Marie Sklodowska-Curie Actions within the *European Union's Horizon* 2020 research and innovation programme under Grant Agreement number 658499 (PolAME). This work has been partially funded by the Spanish Ministry of Economy and Competitiveness (MINECO) under the projects AYA2007-68058-C03-01, AYA2010-21766-C03-02, AYA2012-39475-C02-01, AYA2014-60438-P: ESP2015-70646.C2-1-R, AYA2015-64508-P and the Consolider-Ingenio project CSD2010-00064 (EPI: Exploring the Physics of Inflation). This project has received funding from the European Union's Horizon 2020 research and innovation programme under grant agreement number 687312 (RADIOFOREGROUNDS). CD and SH acknowledge support from an ERC Consolidator grant (no. 307209). CD also acknowledges support from an STFC Consolidated grant (ST/L000768/1). We acknowledge the use of data from the *Planck*/ESA mission, downloaded from the *Planck* Legacy Archive, and of the Legacy Archive for Microwave Background Data Analysis (LAMBDA). Support for LAMBDA is provided by the NASA Office of Space Science. Some of the results in this paper have been derived using the HEALPIX (Górski et al. 2005) package. This work made use of the Strasbourg Astronomical Data Center though the CDS digital platform.

REFERENCES

Ali-Haïmoud Y., Hirata C. M., Dickinson C., 2009, MNRAS, 395, 1055
Alina D., Montier L., Ristorcelli I., Bernard J.-P., Levrier F., Abdikamalov E., 2016, A&A, 595, A57
Arce H. G., Goodman A. A., Bastien P., Manset N., Sumner M., 1998, ApJ, 499, L93
Ashton P. C. et al., 2018, ApJ, 857, 10
Bennett C. L. et al., 2013, ApJS, 208, 20
Bonaldi A., Ricciardi S., Leach S., Stivoli F., Baccigalupi C., de Zotti G., 2007, MNRAS, 382, 1791
Cardoso J.-F., Le Jeune M., Delabrouille J., Betoule M., Patanchon G., 2008, IEEE J. Sel. Top. Signal Process., 2, 735
Chapman N. L., Goldsmith P. F., Pineda J. L., Clemens D. P., Li D., Krčo M., 2011, ApJ, 741, 21
Crutcher R. M., Troland T. H., 2008, ApJ, 685, 281
de Oliveira-Costa A., Tegmark M., Page L. A., Boughn S. P., 1998, ApJ, 509, L9
Dickinson C., Davies R. D., Davis R. J., 2003, MNRAS, 341, 369
Dickinson C. et al., 2018, New Astron. Rev., 80, 1
Draine B. T., 2011, Bruce T. Draine, Physics of the Interstellar and Intergalactic Medium , Princeton University Press, Princeton
Draine B. T., Hensley B., 2013, ApJ, 765, 159
Draine B. T., Hensley B. S., 2016, ApJ, 831, 59
Draine B. T., Lazarian A., 1998, ApJ, 508, 157
Draine B. T., Lazarian A., 1999, ApJ, 512, 740
Finkbeiner D. P., 2003, ApJS, 146, 407
Gandilo N. N. et al., 2016, ApJ, 824, 84
Génova-Santos R. et al., 2015, MNRAS, 452, 4169
Génova-Santos R. et al., 2017, MNRAS, 464, 4107
Górski K. M., Hivon E., Banday A. J., Wandelt B. D., Hansen F. K., Reinecke M., Bartelmann M., 2005, ApJ, 622, 759
Hafez Y. A. et al., 2008, MNRAS, 388, 1775
Hanisch R. J., 1984, A&A, 137, 250
Harper S., Dickinson C., Battye R., Roychowdhury S., Browne I., Ma Y.-Z., Olivari L., Chen T., 2018, MNRAS, 478, 2, 2416
Harper S. E., Dickinson C., Cleary K., 2015, MNRAS, 453, 3375
Haslam C. G. T., Salter C. J., Stoffel H., Wilson W. E., 1982, A&AS, 47, 1
Hauser M. G. et al., 1998, ApJ, 508, 25
Hensley B. S., Draine B. T., 2017, ApJ, 836, 179
Hensley B. S., Draine B. T., Meisner A. M., 2016, ApJ, 827, 45
Hoang T., Draine B. T., Lazarian A., 2010, ApJ, 715, 1462
Irfan M. O. et al., 2015, MNRAS, 448, 3572
King O. G. et al., 2014, MNRAS, 438, 2426
Kurki-Suonio H., Keihänen E., Keskitalo R., Poutanen T., Sirviö A.-S., Maino D., Burigana C., 2009, A&A, 506, 1511
Leitch E. M., Readhead A. C. S., Pearson T. J., Myers S. T., 1997, ApJ, 486, L23
Lombardi M., Lada C. J., Alves J., 2010, A&A, 512, A67
Macellari N., Pierpaoli E., Dickinson C., Vaillancourt J. E., 2011, MNRAS, 418, 888
Markwardt C. B., 2009, in Bohlender D. A., Durand D., Dowler P., eds, ASP Conf. Ser. Vol. 411, Astronomical Data Analysis Software and Systems XVIII. Astron. Soc. Pac., San Francisco, p. 251
Orlando E., Strong A., 2013, MNRAS, 436, 2127
Palmeirim P. et al., 2013, A&A, 550, A38
Panopoulou G. V., Tassis K., Goldsmith P. F., Heyer M. H., 2014, MNRAS, 444, 2507
Pineda J. L., Goldsmith P. F., Chapman N., Snell R. L., Li D., Cambrésy L., Brunt C., 2010, ApJ, 721, 686
Planck Collaboration I, 2016b, A&A, 594, A1
Planck Collaboration IX, 2014b, A&A, 571, A9
Planck Collaboration IX, 2016c, A&A, 594, A9
Planck Collaboration X, 2016d, A&A, 594, A10
Planck Collaboration XI, 2014c, A&A, 571, A11
Planck Collaboration XIII, 2014d, A&A, 571, A13
Planck Collaboration XIX, 2015a, A&A, 576, A104
Planck Collaboration XIX, 2016e, A&A, 594, A19
Planck Collaboration XV, 2014a, A&A, 565, A103
Planck CollaborationXX, 2011a, A&A, 536, A20
Planck Collaboration XX, 2015b, A&A, 576, A105
Planck Collaboration XXV, 2011b, A&A, 536, A25
Planck CollaborationXXV, 2016f, A&A, 594, A25
Planck Collaboration XXVI, 2016g, A&A, 594, A26
Planck CollaborationXXXV, 2016a, A&A, 586, A138
Platania P., Bensadoun M., Bersanelli M., De Amici G., Kogut A., Levin S., Maino D., Smoot G. F., 1998, ApJ, 505, 473
Poidevin F. et al., 2018, The QUIJOTE Experiment: Prospects for CMB B-mode polarization detection and foregrounds characterization, Proceeding of the 13th Rencontres du Vietnam 2017, July 9-15, 2017, ICISE, Quy Nhon, Vietnam
Qian L., Li D., Offner S., Pan Z., 2015, ApJ, 811, 71
Reich P., Reich W., 1988, A&AS, 74, 7
Reich P., Reich W., 1986, A&AS, 63, 205
Reich P., Testori J. C., Reich W., 2001, A&A, 376, 861
Reich W., 1982, A&AS, 48, 219
Reich W., Kalberla P., Neidhoefer J., 1976, A&A, 52, 151
Remazeilles M., Dickinson C., Banday A. J., Bigot-Sazy M.-A., Ghosh T., 2015, MNRAS, 451, 4311
Rubiño-Martín J. A. et al., 2012, in Larry M. Stepp L. M. , Gilmozzi R., Hall H. J., eds, in Proc. SPIE Conf. Ser. Vol. 8444, Ground-based and Airborne Telescopes IV. SPIE, Bellingham, p. 84442Y
Rubiño-Martín J. A. et al., 2017, in Arribas S., Alonso-Herrero A., Figueras F., Hernández-Monteagudo C., Sánchez-Lavega A., Pérez-Hoyos S., eds, Highligths on Spanish Astrophysics IX, Proceeding of the XII Scientific Meeting of the Spanish Astronomical Society held on July 18-22, 2016, , in Bilbao, Spain. p. 99
Strong A. W., Orlando E., Jaffe T. R., 2011, A&A, 534, A54
Turtle A. J., Pugh J. F., Kenderdine S., Pauliny-Toth I. I. K., 1962, MNRAS, 124, 297
Vaillancourt J. E., Matthews B. C., 2012, ApJS, 201, 13
Vrba F. J., Rydgren A. E., 1984, ApJ, 283, 123

Downloaded from https://academic.oup.com/mnras/article-abstract/486/1/462/5255197 by CSIC user on 05 June 2020

Vrba F. J., Rydgren A. E., 1985, AJ, 90, 1490
Watson R. A., Rebolo R., Rubiño-Martín J. A., Hildebrandt S., Gutiérrez C. M., Fernández-Cerezo S., Hoyland R. J., Battistelli E. S., 2005, ApJ, 624, L89
Weiland J. L. et al., 2011, ApJS, 192, 19
Wolleben M., Landecker T.L., Reich W., Wielebinski R., 2006, A&A, 448, 411
Wolleben M., Reich W., 2004, A&A, 427, 537
Ysard N., Verstraete L., 2010, A&A, 509, A12
Ysard N. et al., 2013, A&A, 559, A133
Zhang H., Telesco C. M., Hoang T., Li A., Pantin E., Wright C. M., Li D., Barnes P., 2017, ApJ, 844, 6

APPENDIX A: ADDITIONAL NULL TESTS

The full data set has also been divided in two data sets by considering the maps showing back-end module (BEM) averaged temperature values of $\langle T_{\rm BEM}\rangle$ lower and higher than the median value $\langle T_{\rm BEM}\rangle_{\rm MEDIAN}$ of the full data set. The results from this NT analysis are given in Table A1. Similarly the NT results obtained by considering the data sets obtained by splitting the data set into two groups as a function of azimuth are shown in Table A2. One can see good consistency with the results obtained from the NT analysis obtained when considering the first half of the maps observed with the second half as displayed in Table 1.

Table A1. Same as in Table 1 by splitting the full data set in two groups of maps obtained by considering observations with a mean temperature of the BEM, $T_{\rm BEM}$, higher or lower than the BEM median temperature value, $\langle T_{\rm BEM}\rangle_{\rm MEDIAN}$, of the full set of observations.

Horn	Freq. (GHz)	σ_I (μK beam^{-1}) Map	NT	σ_Q (μK beam^{-1}) Map	NT	σ_U (μK beam^{-1}) Map	NT	$\sigma_{Q,U}$ (mK s$^{1/2}$) NT
1	11	45.9	29.8	–	–	–	–	–
1	13	38.5	24.7	–	–	–	–	–
2	17	98.0	62.4	16.1	11.1	15.1	10.5	2.5
2	19	115.0	75.3	21.9	15.6	16.6	12.3	2.6
3	11	70.9	44.5	21.4	13.7	15.1	12.7	2.5
3	13	58.2	36.0	18.7	12.2	16.5	11.4	2.3
4	17	103.4	71.3	18.1	12.7	14.4	11.4	2.3
4	19	122.0	92.9	21.5	14.9	19.3	15.6	2.9

Table A2. Same as in Table 1 with the data set split into two equal group sampling about the same azimuth and elevation ranges.

Horn	Freq. (GHz)	σ_I (μK beam^{-1}) Map	NT	σ_Q (μK beam^{-1}) Map	NT	σ_U (μK beam^{-1}) Map	NT	$\sigma_{Q,U}$ (mK s$^{1/2}$) NT
1	11	45.9	34.1	–	–	–	–	–
1	13	38.5	29.1	–	–	–	–	–
2	17	98.0	63.7	16.1	11.6	15.1	11.0	2.6
2	19	115.0	66.3	21.9	14.3	16.6	12.4	2.5
3	11	70.9	44.1	21.4	14.1	15.1	12.9	2.6
3	13	58.2	35.9	18.7	12.8	16.5	12.7	2.4
4	17	103.4	71.6	18.1	12.6	14.4	12.0	2.3
4	19	122.0	86.6	21.5	16.6	19.3	13.7	2.8

Downloaded from https://academic.oup.com/mnras/article-abstract/486/1/462/5255197 by CSIC user on 05 June 2020

APPENDIX B: BACKGROUND ASSESSMENT

We conducted several tests to assess whether the area used as the background region captures as accurately as possible an average picture of the ISM properties in the vicinity of the TMC. The level of the variations of the SED fluxes as a function of the areas covered by the TMC and background regions was assessed by checking the effect of changing the limits on A_V used to define the area of the TMC and the background regions shown in Fig. 9. Using $A_V = 4.0$ mag and $A_V = 5.0$ mag produces, to within the uncertainties, fluxes similar to within a few Jy to those that are obtained with a limit value of $A_V = 4.5$ mag at frequencies higher than 10 GHz. Another test to assess the relevance of using the background area displayed in Fig. 9 was done by calculating SEDs of the TMC for various sub-regions of the background area. To do this we calculated the contribution of the background towards apertures of diameter 1.5° on a sample of spatially independent positions displayed over the background region area. These apertures are shown in the A_V maps in Fig. B1. For each aperture an SED of the TMC was calculated; we then estimated the median and the variance of the fluxes at each frequency. These estimates are plotted as a function of frequency in Fig. B2 (top). The relative flux variations obtained from a comparison of the two methods (fluxes calculated by considering the full background area versus the median of the fluxes obtained with the background sampled in the circular apertures) are plotted as a function of frequency in Fig. B2 (bottom). One can see generally good agreement with variations of order 5 per cent or better at the QUIJOTE frequencies (except for one point at 13 GHz) confirming that, at each frequency, the fluxes obtained when the full background area is sampled by circular apertures are statistically consistent with the flux obtained with the full background region. As a final test, we found that the results obtained with SED modelling when using only the QUIJOTE maps from horn 3 are consistent with the SED modelling results obtained when horns 1 and 2 are also included. All in all, we believe that the background region as defined in Fig. 9 and also shown in Fig. B1 (bottom) is good enough to capture the diffuse ISM properties allowing us to calculate the SED of the molecular cloud region with accuracy.

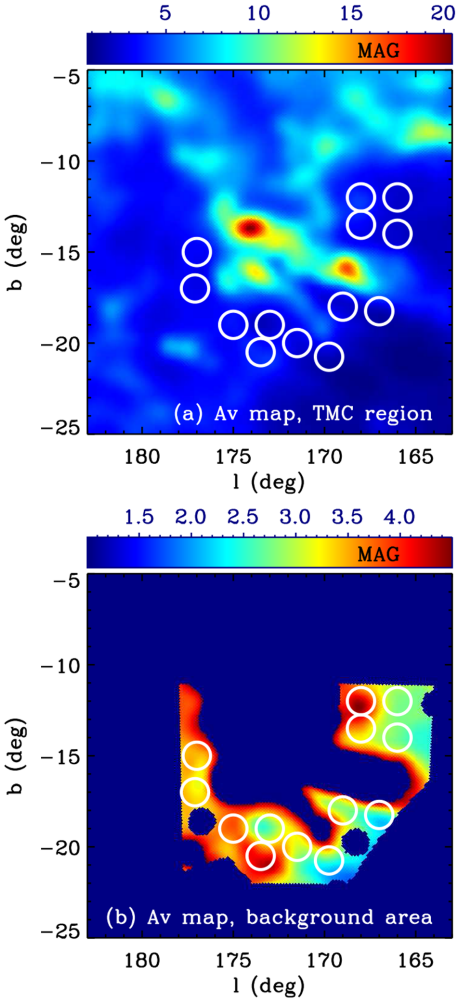

Figure B1. (a) *Planck* A_V map of the TMC and its vicinity. The location of the sample of apertures is shown with white circles. (b) Full background region area used to calculate the fluxes of the TMC displayed in Table 5. The samples of 13 circular apertures used to study the variations of the full background region are delineated by the white circles.

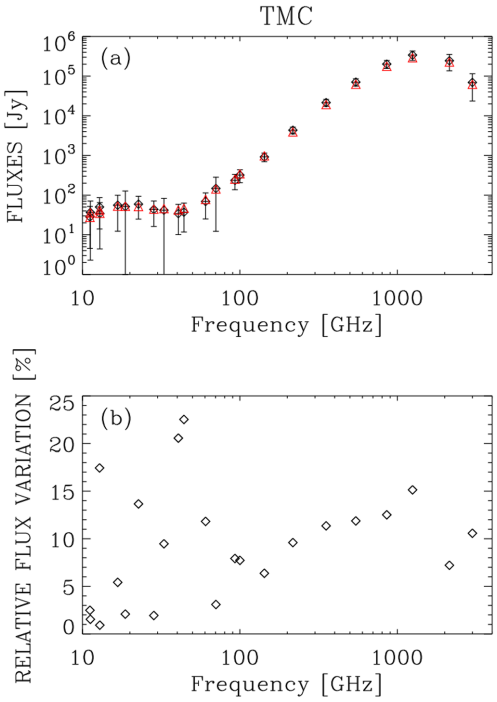

Figure B2. (a) Median values and dispersion of the TMC fluxes obtained when the background is sampled with the 13 circular apertures shown with diamond symbols in Fig. B1 plotted as a function of frequencies. The fluxes obtained towards the TMC with the full background area (see Table 5) are plotted for comparison and shown with red triangles. (b) Relative flux variation between the fluxes displayed in panel (a) as a function of frequency.

This paper has been typeset from a TEX/LATEX file prepared by the author.

Downloaded from https://academic.oup.com/mnras/article-abstract/486/1/462/5255197 by CSIC user on 05 June 2020